Journal of the Mechanics and Physics of Solids 118 (2018) 115–132

Contents lists available at ScienceDirect

Journal of the Mechanics and Physics of Solids

journal homepage: www.elsevier.com/locate/jmps

Bloch wave framework for structures with nonlocal interactions: Application to the design of origami acoustic metamaterials

Phanisri P. Pratapa, Phanish Suryanarayana, Glaucio H. Paulino*

School of Civil and Environmental Engineering, Georgia Institute of Technology, Atlanta, GA 30332, USA

ARTICLE INFO

Article history:
Received 12 April 2018
Revised 14 May 2018
Accepted 15 May 2018

Keywords:
Bloch wave analysis
Acoustic bandgap
Mechanical metamaterials
Origami patterns
Miura-ori
Eggbox pattern

ABSTRACT

We present a generalized Bloch wave framework for the dynamic analysis of structures with nonlocal interactions and apply it to the design of origami acoustic metamaterials. Specifically, we first discretize the origami structures using a customized structural bar-and-hinge model that minimizes the degrees of freedom in the associated unit cell, while being sufficiently accurate to capture the behavior of interest. Next, observing that this discretization results in nonlocal structural interactions—the stiffness matrix has nonzeros between nodes that are not nearest neighbors due to the coupled deformations arising during folding or bending—we generalize the standard Bloch wave approach used in structural analysis to enable the study of such systems. Utilizing this framework, choosing the geometry of the unit cell as well as the folded state of the structure as design variables, we design tunable and programmable Miura-ori and eggbox *strips*, *sheets*, and *composites* that are large band, low frequency acoustic switches. In doing so, we find that the number of bandgaps in the sheets is significantly smaller than their strip counterparts and also occur at relatively higher frequencies, a limitation which is overcome by considering composite structures that have individual panels made of different materials. Overall, we have found origami structures to be ideal candidates as acoustic metamaterials for noise control, vibration isolation, impact absorption, and wave guides.

1. Introduction

Acoustic metamaterials are artificially created systems that are designed to have controlled propagation of elastic or phonon waves (Cummer et al., 2016; Hussein et al., 2014; Maldovan, 2013). Such materials have a number of applications including vibration isolation, impact absorption, noise control, and wave guides. An important characteristic of acoustic metamaterials is the presence—in particular, the size and location—of bandgaps, which represent frequency ranges within which waves cannot propagate in the system. Essentially, bandgaps are associated with the existence of localized resonant modes that cause exponential attenuation and prevent wave propagation at the corresponding frequencies (Baravelli and Ruzzene, 2013; Liu et al., 2000). For practical applications, it is highly desirable to be able to design acoustic metamaterials that are both *tunable*—properties of interest (e.g., bandgap) can be changed in real-time through the application of an active

* Corresponding author.
E-mail address: paulino@gatech.edu (G.H. Paulino).

https://doi.org/10.1016/j.jmps.2018.05.012
0022-5096/

stimulus (e.g., force); and *programmable*—properties of interest (e.g., bandgap) can be changed based on variations in the design (e.g., geometry) without the need to maintain an active stimulus.

Origami-based systems have found a number of scientific and engineering applications. Specifically, spurred by new developments in mathematics (Demaine and O'Rourke, 2007; Lang, 2011), origami has found applications in a wide variety of fields and scales including, for example, graphene folding in nanotechnology (Mu et al., 2015), stent grafts in medicine (Kuribayashi et al., 2006), folding of polymers with light in photonics (Ryu et al., 2012), solar cells (Tang et al., 2014), lithium-ion batteries (Song et al., 2014), self-folding machines (Felton et al., 2014), adaptive building skin structures (Del Grosso and Basso, 2010), active structures (Peraza-Hernandez et al., 2014), and deployment of large membranes in space (Miura, 1985). Notably, origami assemblages also have the potential ability to behave as mechanical metamaterials (Christensen et al., 2015; Silverberg et al., 2014), including topological acoustic metamaterials (Huber, 2016), and thus the realization of such properties is an active area of interest. Indeed, some of these remarkable properties exhibited by origami/kirigami-inspired patterns (Eidini and Paulino, 2015; Schenk and Guest, 2013) are programmable based on their geometry and tunable based on the folded configurational state (Wei et al., 2013). In spite of these substantial advancements, the dynamic behavior of periodic origami systems[1] has not been well studied in the literature, and thus this is the focus of our present investigation.[2]

The study of wave propagation in periodic structures is typically performed using the Bloch wave analysis (Bertoldi and Boyce, 2008; Phani et al., 2006; Ruzzene et al., 2003). In this approach, the translational symmetry of the system is utilized to reduce the problem to the first Brillouin zone in reciprocal or wavevector space (Brillouin, 1953; Kittel, 1966), thereby providing tremendous simplification in the dynamic analysis of such systems. In fact, the topology of the bands during the Bloch wave analysis can also be used to predict the presence of topologically protected waves in finite structures (Pal and Ruzzene, 2017). However, since the Bloch wave analysis involves the solution of an eigenvalue problem at every wavevector of interest, it can be associated with significant computational cost. This is a consequence of the large number of degrees of freedom (e.g., arising within the finite-element method) that are typically required for the discretization of structures displaying novel/exotic properties and the cubic scaling with system size associated with the diagonalization procedure (Suryanarayana, 2013; Suryanarayana et al., 2017). This limitation becomes even more acute in the design of structures with tailored properties since a single design may require hundreds of thousands of Bloch wave analyses. Thus, there is a need for a reduced order model approach, which is addressed here.

In this work, we design origami structures that are tunable and programmable, large band, low frequency acoustic switches. To do so, we first employ a bar-and-hinge model (Filipov et al., 2017; 2015b; Schenk and Guest, 2011) that enables the accurate discretization of origami structures with minimal degrees of freedom. Next, observing that the bar and hinge model results in nonlocal structural interactions—the stiffness matrix has nonzeros between nodes that are not nearest neighbors, a situation arising in origami structures due to the coupled deformations arising during folding or bending—we generalize the standard Bloch wave approach used in structural analysis to enable the study of such systems. We also show how additional symmetries in the system can be used to reduce the analysis to the irreducible Brillouin zone. Utilizing this framework and choosing the geometry of the unit cell as well as the folded state of the structure as design variables, we design tunable and programmable Miura-ori and eggbox *strips, sheets*, and *composites* that are large band, low frequency acoustic switches. In doing so, we demonstrate that the number of bandgaps in Miura-ori and eggbox sheets is significantly smaller than their strip counterparts and also occur at relatively higher frequencies, a limitation which is overcome by considering composite structures that has panels made of different materials.

The remainder of this paper is organized as follows. First, we describe the geometry of origami structures, their discretization using the bar-and-hinge model and the resulting nonlocal nature of the system in Section 2. Next, we develop the generalized Bloch wave theory that is suitable for systems with nonlocal interactions in Section 3. Subsequently, we utilize the developed framework to design origami acoustic metamaterials in Section 4. Finally, we present concluding remarks in Section 5.

2. Structural analysis of origami

In this section, we describe the framework adopted for the structural analysis of origami, which forms the basis for the subsequent Bloch wave formulation. First, we discuss the geometry of origami structures. Next, we describe the discretization of origami using the bar-and-hinge model. Finally, we discuss the nonlocal nature of the bar-and-hinge discretization and its implications.

2.1. Geometry of origami

The geometry of origami structures is characterized by crease lines that are either mountain or valley folds. The crease lines include open edges at the boundaries of the structure and within the structure at the locations of any holes or cuts,

[1] It is common to assume that the structure is periodic when it consists of a large number of repeating unit cells and the boundary effects are negligible.

[2] Preliminary studies on composite Miura-ori origami patterns that possess high frequency bandgaps have recently been performed by the authors (Pratapa et al., 2017). In addition, Yasuda et al. (2016) have recently studied wave dynamics of a one-dimensional rigid origami where the origami panels are not allowed to deform. However, the rigid panel assumption is too restrictive because it does not allow wave propagation in periodic lattices. Indeed, panel bending and stretching are expected to play a critical role in the dynamic behavior of origami structures.

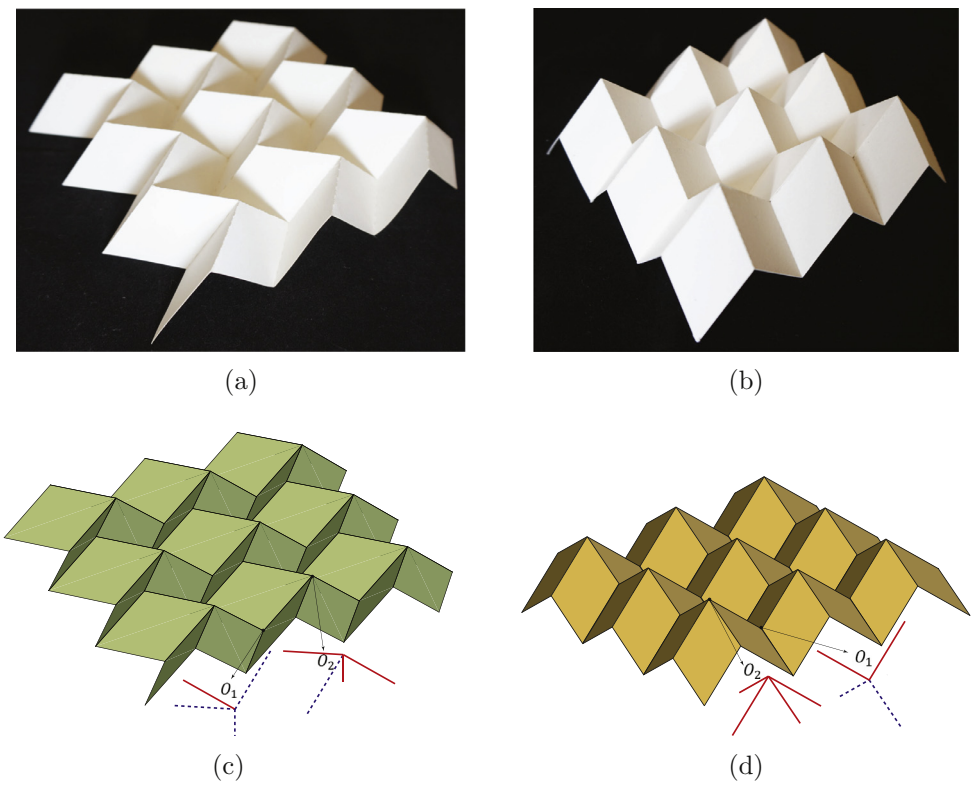

Fig. 1. Examples of origami patterns. (a) and (c) Paper model and corresponding schematic of 3 × 3 Miura-ori pattern. (b) and (d) Paper model and corresponding schematic of 3 × 3 eggbox pattern. The mountain and valley folds around the vertices O_1 and O_2 are shown in solid red and dashed blue lines, respectively. The O_1 and O_2 vertices have equivalent connectivity in Miura-ori (3 mountains and 1 valley; or vice-versa), which is not the case in eggbox (4 mountains or 2 mountains and 2 valleys). (For interpretation of the references to color in this figure legend, the reader is referred to the web version of this article.)

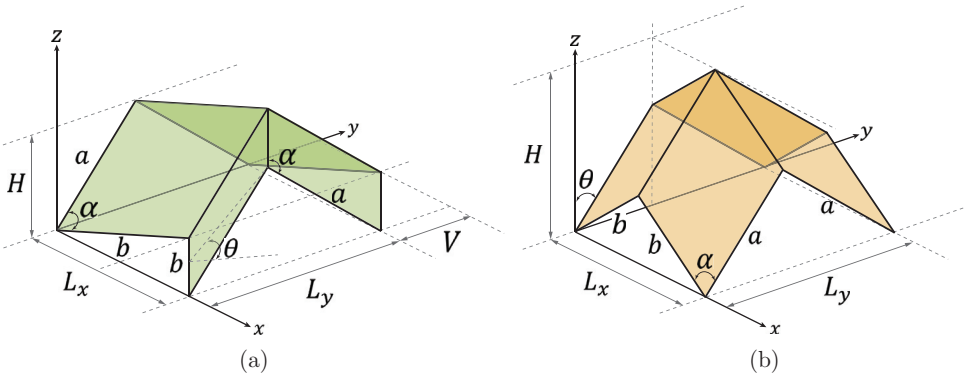

Fig. 2. Parametrization of origami unit cell geometries. (a) Miura-ori. (b) Eggbox.

e.g., kirigami. The polygons resulting from the crease/fold lines (or edges) are called panels and the points at which the fold lines meet are called vertices. Origami structures possess many desirable properties for practical applications, including developability and flat-foldability (ORourke, 2011). The former enables folding of a structure from a single sheet of material and the latter enables compressing the structure into a highly compact volume. The origami structures of interest in this work (see Fig. 1 for Miura-ori and eggbox examples) will be investigated with special attention to such type of properties.

The Miura-ori pattern is developable and is flat-foldable in one of the tessellation directions. It is formed from quadrilateral panels and has a four-vertex geometry (Waitukaitis and van Hecke, 2016), wherein each vertex is formed by the intersection of four crease lines. Notably, every vertex is equivalent and is formed by the intersection of three mountain (or valley) folds and one valley (or mountain) fold. The geometry of the Miura-ori unit cell is shown in Fig. 2a, whose

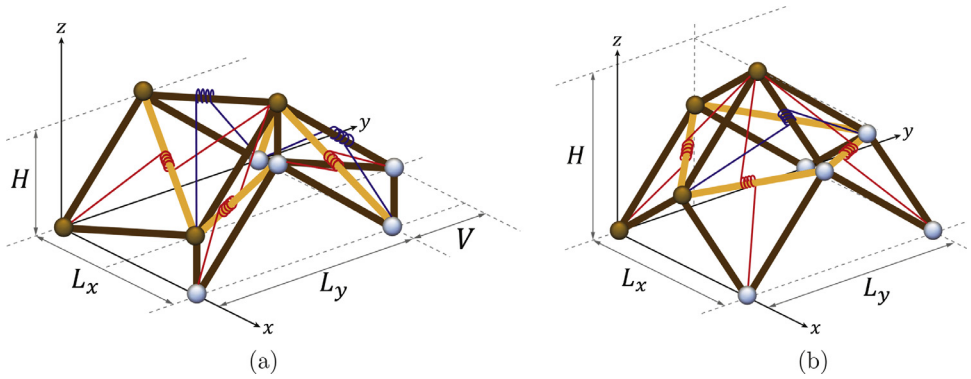

Fig. 3. Examples of the bar-and-hinge representation of the origami unit cells. The bars along the fold lines are represented in a darker color and the bars along the bending creases are in a lighter shade. The nodes (pin joints) are depicted using solid spheres. Nodes in darker color belong to the unit cell that is shown, and those in lighter color belong to the neighboring unit cells. For visual clarity, the rotational springs associated with the bending creases (in red) and fold lines (in blue) are shown only for some bars. (a) Miura-ori pattern. (b) Eggbox pattern. (For interpretation of the references to color in this figure legend, the reader is referred to the web version of this article.)

dimensions H, L_x, and L_y can be expressed as (Schenk and Guest, 2013):

$$H = a\sin\theta\sin\alpha\,, \quad L_y = 2a\sqrt{1-\sin^2\theta\sin^2\alpha}\,,$$
$$L_x = 2b\frac{\cos\theta\tan\alpha}{\sqrt{1+\cos^2\theta\tan^2\alpha}}\,, \quad V = b\frac{1}{\sqrt{1+\cos^2\theta\tan^2\alpha}}\,, \tag{1}$$

where a and b are the edge lengths, α is the panel angle, and θ is the folding/control angle. Note that as θ varies from 0° to 90°, the Miura-ori structure goes from flat to a fully folded state.

The eggbox structure is not developable, but is flat-foldable in both the tessellation directions. Similar to the Miura-ori, it is also formed from quadrilateral panels and has a four-vertex geometry. However, the eggbox has two types of vertices: (i) intersection of either four mountain folds or four valley folds, and (ii) intersection of two mountain and two valley folds. The geometry of the eggbox unit cell is shown in Fig. 2b, whose dimensions H, L_x, and L_y can be expressed as (Schenk, 2011):

$$H = a\cos\theta + b\frac{\cos\alpha}{\cos\theta}\,, \quad L_x = 2b\sqrt{1-\frac{\cos^2\alpha}{\cos^2\theta}}\,, \quad L_y = 2a\sqrt{1-\cos^2\theta}\,, \tag{2}$$

where a and b are the edge lengths, α is the panel angle, and θ is the folding/control angle. Note that θ can only vary from 0° to α, as the patterns goes from one flat folded state to the other.

2.2. Structural discretization: bar-and-hinge model

A structural model involving bars and hinges has recently been proposed for studying the mechanical behavior of origami (Schenk and Guest, 2011). In this formulation, the entire origami structure is modeled as a set of bars (similar to truss members) connected through pin joints, with the folding motion modeled as a compliant mechanism using rotational hinges about the bars. In relation to the continuous structure, bars represent the fold lines formed by the edges of the panels and pin joints (or nodes) denote the vertices. Further, in order to provide in-plane stability and enable bending of panels, the polygonal panels are triangulated with bars. The compliant rotation about the fold lines and the bending of the panels is modeled through rotational hinges/springs with different stiffnesses. Overall, the deformation characteristics of the structure depend on the extensions of the bars as well as the relative rotations of the triangular panels about the fold lines or bending creases. The bar-and-hinge representations of the Miura-ori and eggbox unit cells are shown in Fig. 3.

In the bar-and-hinge model, we have (Filipov et al., 2017; 2015b; Schenk and Guest, 2011)

$$\begin{bmatrix}\mathbf{C}\\ \mathbf{J}_b\\ \mathbf{J}_f\end{bmatrix}\mathbf{u} = \begin{bmatrix}\mathbf{e}\\ \boldsymbol{\Phi}_b\\ \boldsymbol{\Phi}_f\end{bmatrix}, \tag{3}$$

where $\mathbf{u}$ represents the nodal displacements; $\mathbf{e}$ denotes the bar extensions; $\mathbf{C}$ denotes the compatibility matrix that relates $\mathbf{e}$ to $\mathbf{u}$; $\boldsymbol{\Phi}_b$ and $\boldsymbol{\Phi}_f$ are the rotations associated with the bending creases and fold lines, respectively; and $\mathbf{J}_b$ and $\mathbf{J}_f$ are the rotation compatibility matrices that relate $\boldsymbol{\Phi}_b$ and $\boldsymbol{\Phi}_f$ to $\mathbf{u}$, respectively. Assuming linear elasticity, the constitutive relation for the system can be expressed as

$$\begin{bmatrix}\mathbf{K}_e & 0 & 0\\ 0 & \mathbf{K}_b & 0\\ 0 & 0 & \mathbf{K}_f\end{bmatrix}\begin{bmatrix}\mathbf{e}\\ \boldsymbol{\Phi}_b\\ \boldsymbol{\Phi}_f\end{bmatrix} = \begin{bmatrix}\mathbf{t}\\ \mathbf{m}_b\\ \mathbf{m}_f\end{bmatrix}, \tag{4}$$

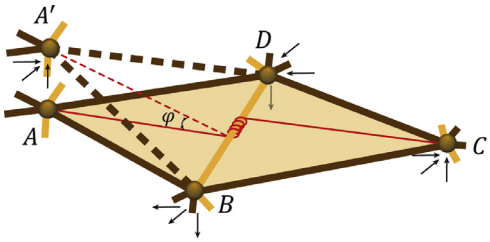

Fig. 4. Schematic representation of the nonlocal structural interactions in the bar-and-hinge model for panel (shaded) bending about the bending crease *BD*. Notice that *AB, BC, CD*, and *DA* are bars corresponding to fold lines along the panel (shaded) perimeter. The panel bending is represented by the presence of a rotational spring about *BD*, connecting vertices *A* and *C*.

where $\mathbf{K}_e$, $\mathbf{K}_b$, and $\mathbf{K}_f$ represent the axial stiffness of the bars, rotational stiffness along the bending creases, and rotational stiffness along the fold lines, respectively; and $\mathbf{t}$, $\mathbf{m}_b$, and $\mathbf{m}_f$ are the bar tensions, resisting moment in bending, and resisting moment in folding hinges, respectively. Using the principle of virtual work, the total external forces on the nodes can be written as

$$\mathbf{f}_{ext} = \mathbf{K}\mathbf{u} = \begin{bmatrix}\mathbf{C}^T & \mathbf{J}_b^T & \mathbf{J}_f^T\end{bmatrix}\begin{bmatrix}\mathbf{t}\\ \mathbf{m}_b\\ \mathbf{m}_f\end{bmatrix}, \tag{5}$$

where $\mathbf{K}$ is the stiffness matrix of the system. It follows from Eqs. (3)–(5) that the stiffness matrix for the origami structure can be written as

$$\mathbf{K} = \begin{bmatrix}\mathbf{C}^T & \mathbf{J}_b^T & \mathbf{J}_f^T\end{bmatrix}\begin{bmatrix}\mathbf{K}_e & 0 & 0\\ 0 & \mathbf{K}_b & 0\\ 0 & 0 & \mathbf{K}_f\end{bmatrix}\begin{bmatrix}\mathbf{C}\\ \mathbf{J}_b\\ \mathbf{J}_f\end{bmatrix} = \mathbf{C}^T\mathbf{K}_e\mathbf{C} + \mathbf{J}_b^T\mathbf{K}_b\mathbf{J}_b + \mathbf{J}_f^T\mathbf{K}_f\mathbf{J}_f\,. \tag{6}$$

In this framework, the mass matrix $\mathbf{M}$ is constructed through the lumped mass approximation, wherein the mass of the triangular panels is distributed uniformly to its three vertices.[3]

In this work, we have chosen the above described bar-and-hinge model since it provides an excellent compromise between accuracy and efficiency. On the one hand, numerical methods like those using shell finite-elements (Ota et al., 2016) are expected to be more accurate and provide more detailed information than the bar-and-hinge model. However, such approaches involve extensive meshing that results in a large number of degrees of freedom. Consequently, such discretizations are associated with large computational expense (Ota et al., 2016), particularly in the Bloch wave based design of origami structures, which involves the repeated solution of eigenvalue problems—a process that scales cubically with the size of the matrix (Pratapa and Suryanarayana, 2016; Suryanarayana, 2013)—during the design process. On the other hand, the assumption of rigid origami can be employed to further reduce the degrees of freedom compared to the bar-and-hinge model, e.g., α, a, b, and θ are sufficient to characterize the deformation in the case of Miura-ori and eggbox structures. However, given the finite stiffness of the origami structure and the associated bending of the panels in practical applications, such an approximation is too restrictive. This is particularly the case for Bloch wave analysis, wherein the rigid origami assumption may be incompatible with the need to admit inhomogeneous deformations, e.g., Miura-ori (Evans et al., 2015).

2.3. Nonlocal structural interactions within the bar-and-hinge model

The stiffness matrix for origami in the bar-and-hinge model consists of three terms, as shown in Eq. (6). This differs from the conventional truss model, wherein the stiffness matrix is comprised of only the first term ($\mathbf{C}^T\mathbf{K}_e\mathbf{C}$). Specifically, incorporation of the rotational stiffness along the bending creases and fold lines in the bar-and-hinge model results in the second ($\mathbf{J}_b^T\mathbf{K}_b\mathbf{J}_b$) and third ($\mathbf{J}_f^T\mathbf{K}_f\mathbf{J}_f$) terms, respectively. Consequently, the resulting stiffness matrix is inherently nonlocal, i.e., the structural interactions extend beyond the nearest neighbor nodes. This can be understood through the schematic in Fig. 4, which depicts the single panel bending about a bending crease in the bar-and-hinge model. Specifically, *BD* is a bar corresponding to the bending crease, with a rotational spring connecting nodes *A* and *C*. A small displacement of the node from *A* to *A′* will induce non-zero forces at all the nodes of the panel. This includes a force on the non-nearest node *C*, arising due to the change in angle ϕ of the rotational hinge. As a consequence of the inherent nonlocality of structural interactions in the bar-and-hinge model, the Bloch wave analysis needs to be suitably generalized, as discussed in the next section.

[3] In general, within the specific scope of the bar-and-hinge model, we have found that the results we present in this paper are qualitatively insensitive to the mass lumping scheme.

3. Bloch wave framework for systems with nonlocal structural interactions

The free wave propagation of a discretized structural system is governed by the generalized eigenvalue problem

$$\mathbf{K}\mathbf{u} = \omega^2 \mathbf{M}\mathbf{u}\,, \tag{7}$$

where $\mathbf{K}$ is the stiffness matrix, $\mathbf{u}$ is a vector of nodal displacements, ω is the frequency of harmonic wave propagation, and $\mathbf{M}$ is the mass matrix. In structures which possess a unit cell that repeats, it is common to neglect the effect of the boundaries (i.e., assume infinite extent) and perform a Bloch wave reduction of the eigenvalue problem in Eq. (7) to the unit cell/fundamental domain. Since solution of an eigenvalue problem scales cubically with the size of the system, the Bloch wave approach not only significantly reduces the computational expense, but also provides a simplified framework for the interpretation of results. However, the commonly employed structural Bloch wave analysis (Gonella and Ruzzene, 2008; Mousanezhad et al., 2015; Phani et al., 2006; Ruzzene et al., 2003) is restricted to systems with local interactions, i.e., only the nearest node components of the stiffness matrix are non-zero. In view of this, we now generalize the Bloch wave analysis such that it is applicable to systems with nonlocal interactions, e.g., origami structures discretized using the bar-and-hinge model. Though such a framework has previously been proposed for atomistic systems (Aghaei et al., 2013), to the best of our knowledge its adaptation for structural systems has not been performed heretofore.

3.1. Bloch wave reduction: Brillouin zone

Consider a periodic system consisting of N unit cells in each of the three coordinate system directions,[4] with M degrees of freedom (DOF) per unit cell. Choosing the origin of the coordinate system to be located at the corner of the central unit cell, the position of the $\mathbf{n}^{th}$ unit cell can be written as[5]

$$\mathbf{x}_{\mathbf{n}} = \mathbf{x}_{(n_1,n_2,n_3)} = n_1\mathbf{a}_1 + n_2\mathbf{a}_2 + n_3\mathbf{a}_3\,, \tag{8}$$

where $n_1, n_2,$ and $n_3 \in \{-(N-1)/2, -(N-3)/2, \ldots, (N-3)/2, (N-1)/2\}$. In addition, $\mathbf{a}_1$, $\mathbf{a}_2$, $\mathbf{a}_3 \in \mathbb{R}^3$ denote the lattice vectors of the structure. The corresponding reciprocal lattice vectors satisfy the relation $\mathbf{a}_i.\mathbf{b}_j = 2\pi\delta_{ij}$, $i, j = \{1, 2, 3\}$, from which we can arrive at the following representation in terms of the lattice vectors[6]:

$$\mathbf{b}_1 = 2\pi\frac{\mathbf{a}_2\times\mathbf{a}_3}{\mathbf{a}_1\cdot(\mathbf{a}_2\times\mathbf{a}_3)}\,,\quad \mathbf{b}_2 = 2\pi\frac{\mathbf{a}_3\times\mathbf{a}_1}{\mathbf{a}_1\cdot(\mathbf{a}_2\times\mathbf{a}_3)}\,,\quad \mathbf{b}_3 = 2\pi\frac{\mathbf{a}_1\times\mathbf{a}_2}{\mathbf{a}_1\cdot(\mathbf{a}_2\times\mathbf{a}_3)}\,. \tag{9}$$

In Fig. 5, we illustrate this framework for a bar-and-hinge discretized Miura-ori and eggbox patterns, which form 2D lattices.

Let $\mathbf{u}_{(\mathbf{n},\,\ell)}$ denote the displacement along the ℓth DOF in the $\mathbf{n}$th unit cell. If we assume the displacement to be periodic across the system, i.e., $\mathbf{u}_{(\mathbf{n}+\mathbf{N},\ell)} = \mathbf{u}_{(\mathbf{n},\ell)}$, where $\mathbf{N} = (N, N, N)$ defines the periodicity of the structure, we can define the Discrete Fourier Transform of $\mathbf{u}_{(.,\ell)} \in \mathbb{R}^{N^3}$ (for each DOF ℓ) and corresponding inverse Discrete Fourier Transform as

$$\tilde{\mathbf{u}}_{(\mathbf{m},\ell)} = \frac{1}{\sqrt{N^3}}\sum_{\mathbf{n}=-(\mathbf{N}-\mathbf{1})/2}^{(\mathbf{N}-\mathbf{1})/2} e^{i\mathbf{k}_{\mathbf{m}}.\mathbf{x}_{\mathbf{n}}}\mathbf{u}_{(\mathbf{n},\ell)}\,,\quad \mathbf{u}_{(\mathbf{n},\ell)} = \frac{1}{\sqrt{N^3}}\sum_{\mathbf{m}=-(\mathbf{N}-\mathbf{1})/2}^{(\mathbf{N}-\mathbf{1})/2} e^{-i\mathbf{k}_{\mathbf{m}}.\mathbf{x}_{\mathbf{n}}}\tilde{\mathbf{u}}_{(\mathbf{m},\ell)}\,. \tag{10}$$

Above, $\mathbf{k}_{\mathbf{m}}$ denotes the wavevector, which can be expressed in terms of the reciprocal lattice vectors as

$$\mathbf{k}_{\mathbf{m}} = \frac{m_1}{N}\mathbf{b}_1 + \frac{m_2}{N}\mathbf{b}_2 + \frac{m_3}{N}\mathbf{b}_3\,, \tag{11}$$

where $m_1, m_2,$ and $m_3 \in \{-(N-1)/2, -(N-3)/2, \ldots, (N-3)/2, (N-1)/2\}$. For the square lattices shown in Fig. 5a and b, the wavevectors are restricted to within the area enclosed by $\{Q'', Q', Q, R'\}$ in Fig. 5c. In matrix representation, Eq. (10) takes the form

$$\tilde{\mathbf{u}} = \mathbf{F}\mathbf{u}\,,\quad \mathbf{u} = \mathbf{F}^{-1}\tilde{\mathbf{u}}\,, \tag{12}$$

where $\mathbf{F} \in \mathbb{C}^{MN^3\times MN^3}$ is the Discrete Fourier Transform matrix.

On left multiplying Eq. (7) by $\mathbf{F}$ and utilizing the unitary property of $\mathbf{F}$ (i.e., $\mathbf{F}\mathbf{F}^{*\mathrm{T}} = \mathbf{F}^{*\mathrm{T}}\mathbf{F} = \mathbf{I}$, where the symbol * represents the conjugate and $\mathbf{I}$ is the identity matrix), we arrive at

$$\tilde{\mathbf{K}}\tilde{\mathbf{u}} = \omega^2\tilde{\mathbf{M}}\tilde{\mathbf{u}}\,,\ \text{where } \tilde{\mathbf{K}} = \mathbf{F}\mathbf{K}\mathbf{F}^{*\mathrm{T}} \text{ and } \tilde{\mathbf{M}} = \mathbf{F}\mathbf{M}\mathbf{F}^{*\mathrm{T}}\,. \tag{13}$$

Due to the translational symmetry in the system, the stiffness and mass matrices ($\mathbf{K}$ and $\mathbf{M}$, respectively) are block-circulant and therefore block-diagonalized by the Discrete Fourier Transform matrix $\mathbf{F}$ (Aghaei et al., 2013; Karner et al., 2003; Olson et al., 2014; Rjasanow, 1994; Süsstrunk and Huber, 2016). Consequently, $\tilde{\mathbf{K}} \in \mathbb{C}^{MN^3\times MN^3}$ and $\tilde{\mathbf{M}} \in \mathbb{C}^{MN^3\times MN^3}$ are block-diagonal

[4] We will assume a 3D lattice for deriving the expressions corresponding to the Bloch wave reduction. However, the results are equally applicable to 2D and 1D lattices, albeit with suitable simplifications. Also, without any loss of generality, we will also assume that N is odd. Indeed, the analysis is equally applicable to the case when N is even and when there are different number of unit cells in each of the coordinate directions.

[5] In the case of a 2D lattice: $\mathbf{x}_{\mathbf{n}} = \mathbf{x}_{(n_1,n_2)} = n_1\mathbf{a}_1 + n_2\mathbf{a}_2$. In the case of a 1D lattice: $\mathbf{x}_{\mathbf{n}} = \mathbf{x}_{(n_1)} = n_1\mathbf{a}_1$.

[6] In the case of a 2D lattice: $\mathbf{b}_1 = 2\pi\frac{\mathbf{R}\mathbf{a}_2}{\mathbf{a}_1\cdot\mathbf{R}\mathbf{a}_2}$, $\mathbf{b}_2 = 2\pi\frac{\mathbf{R}\mathbf{a}_1}{\mathbf{a}_2\cdot\mathbf{R}\mathbf{a}_1}$, where $\mathbf{R}$ is the 90 degree rotation matrix. In the case of a 1D lattice, $\mathbf{b}_1 = 2\pi\frac{\mathbf{a}_1}{\mathbf{a}_1\cdot\mathbf{a}_1}$.

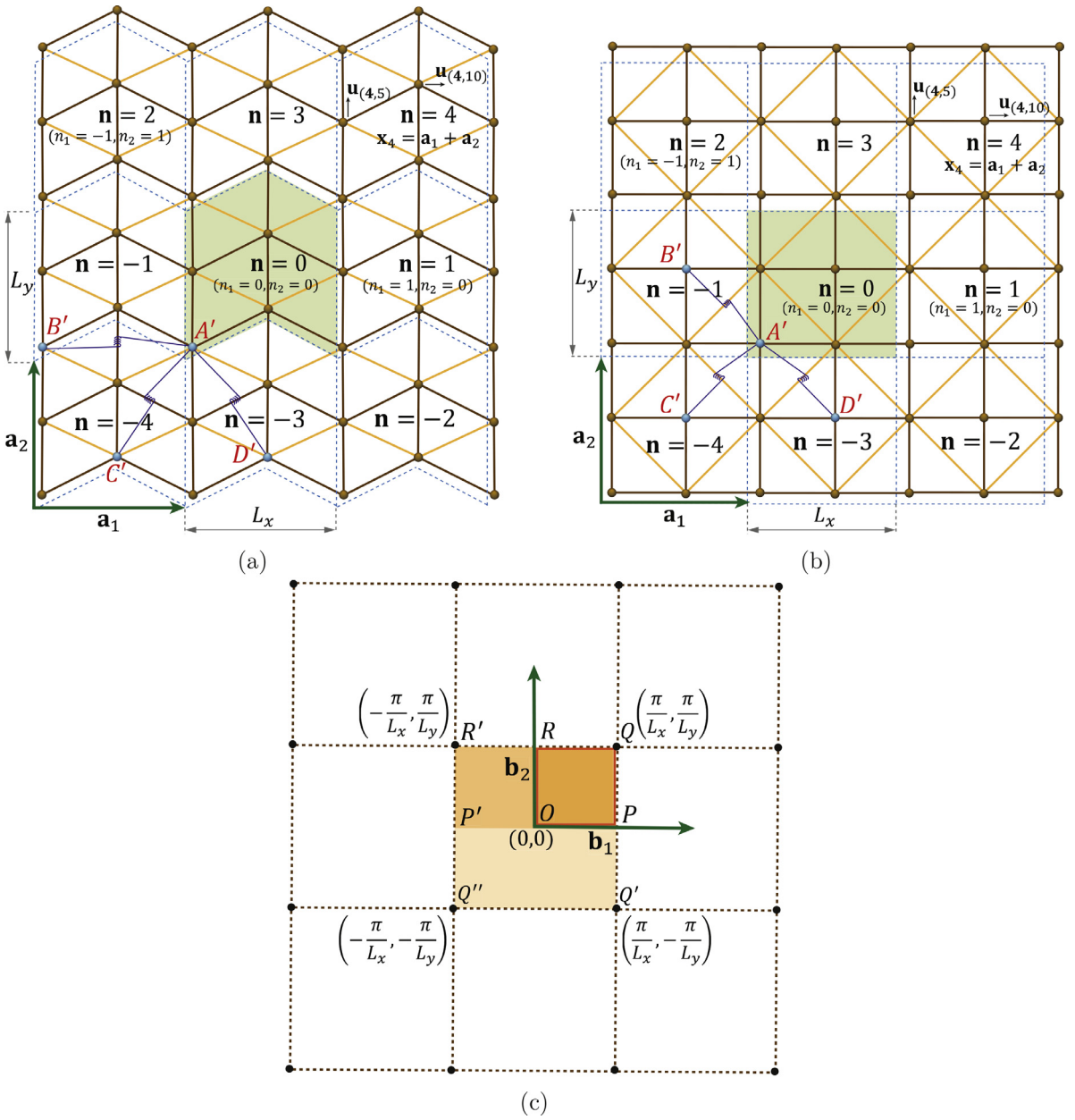

Fig. 5. (a) and (b) Two-dimensional lattices associated to the bar-and-hinge discretization of Miura-ori and eggbox origami patterns, respectively. The dashed lines represent the boundaries of each unit cell within the bar-and-hinge representation. For visual clarity, only the rotational springs associated with nonlocal interactions of node A' are shown. (c) Corresponding reciprocal lattice. The area enclosed by $\{Q'', Q', Q, R'\}$ constitutes the first Brillouin zone, which reduces to the area enclosed by $\{P', P, Q, R'\}$ on applying time-reversal symmetry, which further reduces to the area enclosed by $\{O, P, Q, R\}$ on applying the vertical inversion symmetry. The area enclosed by $\{O, P, Q, R\}$ constitutes the irreducible Brillouin zone (IBZ).

matrices, with the blocks indexed by the wavevector $\mathbf{k_m}$. Since the diagonalization of a block-diagonal matrix is equivalent to the diagonalization of all of its blocks independently, we arrive at an eigenvalue problem for each wavevector $\mathbf{k_m}$:

$$\tilde{\mathbf{K}}_{\mathbf{mm}}\tilde{\mathbf{u}}_{\mathbf{m}} = \omega_m^2 \tilde{\mathbf{M}}_{\mathbf{mm}}\tilde{\mathbf{u}}_{\mathbf{m}}\,, \tag{14}$$

where

$$\tilde{\mathbf{K}}_{\mathbf{mm}} = \sum_{\mathbf{n}=-(\mathbf{N}-\mathbf{1})/2}^{(\mathbf{N}-\mathbf{1})/2} e^{-\mathrm{i}\mathbf{k_m}.\mathbf{x_n}}\mathbf{K_{0n}}\,, \qquad \tilde{\mathbf{M}}_{\mathbf{mm}} = \sum_{\mathbf{n}=-(\mathbf{N}-\mathbf{1})/2}^{(\mathbf{N}-\mathbf{1})/2} e^{-\mathrm{i}\mathbf{k_m}.\mathbf{x_n}}\mathbf{M_{0n}}\,. \tag{15}$$

Above, $\tilde{\mathbf{K}}_{\mathbf{mm}} \in \mathbb{C}^{M\times M}$ and $\tilde{\mathbf{M}}_{\mathbf{mm}} \in \mathbb{C}^{M\times M}$ correspond to the $\mathbf{m}^{th}$ blocks of $\tilde{\mathbf{K}}$ and $\tilde{\mathbf{M}}$, respectively, and correspond to the DOFs within the unit cell. In addition, $\mathbf{K}_{\mathbf{ij}} \in \mathbb{R}^{M\times M}$ (or $\mathbf{M}_{\mathbf{ij}} \in \mathbb{R}^{M\times M}$) is a matrix extracted from $\mathbf{K}$ (or $\mathbf{M}$) with rows corresponding to the DOFs of $\mathbf{i}^{th}$ unit cell and columns corresponding to the DOFs of $\mathbf{j}^{th}$ unit cell. Overall, the free wave propagation problem on the entire structure has been reduced to a single unit cell, with $\tilde{\mathbf{K}}_{\mathbf{mm}}$ and $\tilde{\mathbf{M}}_{\mathbf{mm}}$ being the reduced stiffness and mass matrices corresponding to the wavevector $\mathbf{k}_{\mathbf{m}}$.

In the above analysis, the case of particular interest is $N\to\infty$, which corresponds to the periodic infinite structure. In this limit, rather than the wavevector taking discrete values as given by Eq. (11), it starts taking a continuum of values, the volume[7] of which is referred to as the first Brillouin zone. For example, for the square lattice shown in Fig. 5, the first Brillouin zone is the area enclosed by $\{Q'', Q', Q, R'\}$. Therefore, the original eigenvalue problem of an infinite structure has been reduced to an eigenvalue problem corresponding to the unit cell for infinitely many wavevectors. However, the behavior of the structure typically has a smooth variation in reciprocal space, thereby enabling a thorough analysis even though a finite set of wavevectors is chosen. Finally, we note that unlike the Bloch wave analysis commonly adopted for structural systems, the above described framework is also applicable to systems in which the stiffness and mass matrices have further than nearest node interaction. We demonstrate the need for such a framework through a 1D spring-mass system in Appendix A.

3.2. Symmetry based reduction of Brillouin zone: irreducible Brillouin zone

In addition to the translational symmetry, it is common for additional symmetries (e.g., rotation, mirror) to exist in the system. In such cases, the Bloch wave analysis described above can be further simplified, as described below.

3.2.1. Time-reversal symmetry

Consider the Bloch reduced stiffness and mass matrices at the wavevector $\mathbf{k}_{\mathbf{m}'} = -\mathbf{k}_{\mathbf{m}} = \mathbf{k}_{(-\mathbf{m})}$, i.e., $\tilde{\mathbf{K}}_{\mathbf{m}'\mathbf{m}'}$ and $\tilde{\mathbf{M}}_{\mathbf{m}'\mathbf{m}'}$, respectively. In the case of real-valued symmetric stiffness ($\mathbf{K}$) and mass ($\mathbf{M}$) matrices, we can show:

$$\tilde{\mathbf{K}}_{\mathbf{m}'\mathbf{m}'} = \sum_{\mathbf{n}=-\infty}^{\infty} e^{-\mathrm{i}\mathbf{k}_{(-\mathbf{m})}\cdot\mathbf{x}_{\mathbf{n}}}\mathbf{K}_{\mathbf{0n}} = \sum_{\mathbf{n}=-\infty}^{\infty} e^{-\mathrm{i}\mathbf{k}_{\mathbf{m}}\cdot\mathbf{x}_{(-\mathbf{n})}}\mathbf{K}^{\mathrm{T}}_{\mathbf{0}(-\mathbf{n})} = \tilde{\mathbf{K}}^{\mathrm{T}}_{\mathbf{mm}} = \tilde{\mathbf{K}}^{*}_{\mathbf{mm}}\,, \tag{16}$$

$$\tilde{\mathbf{M}}_{\mathbf{m}'\mathbf{m}'} = \sum_{\mathbf{n}=-\infty}^{\infty} e^{-\mathrm{i}\mathbf{k}_{(-\mathbf{m})}\cdot\mathbf{x}_{\mathbf{n}}}\mathbf{M}_{\mathbf{0n}} = \sum_{\mathbf{n}=-\infty}^{\infty} e^{-\mathrm{i}\mathbf{k}_{\mathbf{m}}\cdot\mathbf{x}_{(-\mathbf{n})}}\mathbf{M}^{\mathrm{T}}_{\mathbf{0}(-\mathbf{n})} = \tilde{\mathbf{M}}^{\mathrm{T}}_{\mathbf{mm}} = \tilde{\mathbf{M}}^{*}_{\mathbf{mm}}\,. \tag{17}$$

Above, we have utilized the relations: $\mathbf{K}_{\mathbf{0n}} = \mathbf{K}^{\mathrm{T}}_{\mathbf{n0}}$ and $\mathbf{M}_{\mathbf{0n}} = \mathbf{M}^{\mathrm{T}}_{\mathbf{n0}}$, which follow from the symmetry of $\mathbf{K}$ and $\mathbf{M}$, respectively. We have also used the relations: $\mathbf{K}_{\mathbf{n0}} = \mathbf{K}_{\mathbf{0}(-\mathbf{n})}$, $\mathbf{M}_{\mathbf{n0}} = \mathbf{M}_{\mathbf{0}(-\mathbf{n})}$, which follows from the block circulant nature of $\mathbf{K}$ and $\mathbf{M}$, respectively. It follows from Eqs. (16) and (17) that $\omega_{m'} = \omega_m$ and $\tilde{\mathbf{u}}_{\mathbf{m}'} = \tilde{\mathbf{u}}^{*}_{\mathbf{m}}$.

This above reduction is attributed to time-reversal symmetry,[8] by virtue of which it is sufficient to consider half of the Brillouin zone to infer the behavior of the structure in the complete Brillouin zone. This can be interpreted as inversion symmetry in reciprocal space. For example, for the square lattices shown in Fig. 5, the first Brillouin zone enclosed by $\{Q'', Q', Q, R'\}$ reduces to the area enclosed by $\{P', P, Q, R'\}$. Note that in order for the system to have time-reversal symmetry, both $\mathbf{K}$ and $\mathbf{M}$ need to be real-valued. This is typically the case for structural systems. However, the presence of active elements (e.g., gyroscopes) can lead to complex-valued matrices, resulting in the breaking of time-reversal symmetry (Nash et al., 2015; Wang et al., 2015).

3.2.2. Spatial symmetry

Consider a symmetry operation of the structure that leaves the structure invariant, with the unit cell located at $\mathbf{x}_{\mathbf{n}}$ mapped to $\mathbf{x}_{\mathbf{n}'}$. Let the corresponding symmetry operation in reciprocal space map the wavevector $\mathbf{k}_{\mathbf{m}}$ to $\mathbf{k}_{\mathbf{m}'}$. Denoting the matrix representation of the symmetry operation for the unit cell by $\mathbf{S} \in \mathbb{R}^{M\times M}$, it follows that

$$\mathbf{S}\tilde{\mathbf{K}}_{\mathbf{mm}}\mathbf{S}^{\mathrm{T}} = \sum_{\mathbf{n}=-\infty}^{\infty} e^{-\mathrm{i}\mathbf{k}_{\mathbf{m}'}\cdot\mathbf{x}_{\mathbf{n}'}}\mathbf{S}\mathbf{K}_{\mathbf{0n}}\mathbf{S}^{\mathrm{T}} = \sum_{\mathbf{n}'=-\infty}^{\infty} e^{-\mathrm{i}\mathbf{k}_{\mathbf{m}'}\cdot\mathbf{x}_{\mathbf{n}'}}\mathbf{K}_{\mathbf{0n}'} = \tilde{\mathbf{K}}_{\mathbf{m}'\mathbf{m}'}\,. \tag{18}$$

$$\mathbf{S}\tilde{\mathbf{M}}_{\mathbf{mm}}\mathbf{S}^{\mathrm{T}} = \sum_{\mathbf{n}=-\infty}^{\infty} e^{-\mathrm{i}\mathbf{k}_{\mathbf{m}'}\cdot\mathbf{x}_{\mathbf{n}'}}\mathbf{S}\mathbf{M}_{\mathbf{0n}}\mathbf{S}^{\mathrm{T}} = \sum_{\mathbf{n}'=-\infty}^{\infty} e^{-\mathrm{i}\mathbf{k}_{\mathbf{m}'}\cdot\mathbf{x}_{\mathbf{n}'}}\mathbf{M}_{\mathbf{0n}'} = \tilde{\mathbf{M}}_{\mathbf{m}'\mathbf{m}'}\,, \tag{19}$$

where we have used the properties: $\mathbf{K}_{\mathbf{0n}'} = \mathbf{S}\mathbf{K}_{\mathbf{0n}}\mathbf{S}^{\mathrm{T}}$ and $\mathbf{M}_{\mathbf{0n}'} = \mathbf{S}\mathbf{M}_{\mathbf{0n}}\mathbf{S}^{\mathrm{T}}$. Consequently, it follows that $\omega_{m'} = \omega_m$ and $\tilde{\mathbf{u}}_{\mathbf{m}'} = \mathbf{S}\tilde{\mathbf{u}}_{\mathbf{m}}$.

[7] Area and length in the case of a 2D and 1D lattices, respectively.

[8] Time-reversal symmetry leads to reciprocity in wave propagation (Cummer et al. (2016)). The terminology has its origins in quantum mechanics where reversing time is equivalent to reversing momentum and hence the wavevector (Gottfried and Yan, 2013).

In view of the above, the Bloch wave analysis does not need to be performed for wavevectors that are related to other wavevectors through the non-trivial spatial symmetries present in the unit cell. After considering time-reversal and spatial symmetries, the smallest region of the Brillouin zone from which the structural behavior at any wavevector can be determined is referred to as the irreducible Brillouin zone. For example, for the square lattices shown in Fig. 5, the first Brillouin zone enclosed by $\{Q'', Q', Q, R'\}$ reduces to the area enclosed by $\{O, P, Q, R\}$ on applying time-reversal symmetry and vertical inversion symmetries. Overall, the above framework can be utilized to make the Bloch wave analysis more simple and efficient by exploiting the symmetry in the structure.

4. Design of origami acoustic metamaterials

We now employ the framework described in the previous two sections to design Miura-ori and eggbox acoustic metamaterials. For this purpose, we develop an implementation[9] of the above described framework in which the origami structure is discretized using the bar-and-hinge model, and the Bloch wave analysis is performed by solving the generalized Hermitian eigenproblem given in Eq. (14) using the QR method. While doing so, rather than adopt the common strategy of only considering wavevectors along the edges of the irreducible Brillouin zone (IBZ), we sample the entire Brillouin zone (BZ) to ensure that the bandgaps are accurately calculated (Kerszberg and Suryanarayana, 2015). In all the simulations, we fix the edge length to be $a = 1$ and the stiffnesses to be $K_f = 1$, $K_b = 10$, and $K_e = 10^5$ (Filipov et al., 2015a). While presenting the results, we normalize the frequencies as $\hat{\omega} = \omega/\omega_0$, where $\omega_0 = \sqrt{K_e/aM_p}$, with M_p being the mass of the quadrilateral panel.

We design the Miura-ori and eggbox structures using genetic algorithms. Since we are interested in programmable and tunable, large band, low frequency acoustic switches, we choose the objective function to be the bandgap between successive bands for all bands, with α, b, and θ being the design variables.[10] The following constraints are imposed on the design variables: (i) $5° \leq \alpha \leq 85°$, $5° \leq \theta \leq 85°$, and $1 \leq b \leq 5$ for Miura-ori, and (ii) $5° \leq \theta \leq 85°$, $5° \leq \alpha \leq 85°$, $\theta \leq \alpha$, and $1 \leq b \leq 5$ for eggbox. Thereafter, among all the structures so obtained, we denote the optimized structure to be the one that results in the lowest frequency bandgap, with a threshold size of 0.15.[11] This optimized structure is then studied for its programmibility (variation with respect to α and b) and tunability (i.e., variation with respect to θ) as acoustic switches.

4.1. Miura-ori and eggbox strips

We first start with the design of Miura-ori and eggbox strips shown in Fig. 6, which also shows the projected nodal unit cell representations and the associated lumped masses. For both structures, the unit cell contains $M = 6$ nodes and therefore 18 DOFs. The IBZ consists of the interval $[0, \pi/L_x]$, by virtue of the structures being periodic in the x-direction and possessing time-reversal symmetry. On performing a preliminary Bloch wave analysis, we have found that the lower modes predominantly consist of bending and folding deformations, whereas the higher modes are dominated by axial deformations.

After utilizing the design process described above, we obtain optimized structures with the following parameters: (i) $\alpha = 64.19°$, $b = 1.09$, and $\theta = 68.64°$ for Miura-ori, and (ii) $\alpha = 69.64°$, $b = 1.4$, and $\theta = 61.87°$ for the eggbox strips, with bandgaps of 0.57 and 0.73 occurring between the fourth and fifth bands,[12] respectively. For these optimized Miura-ori and eggbox structures, we present the tunability of the bandgap size and location[13] in Fig. 7a and d, respectively (bandgap of interest highlighted using a darker shade). Further, in the context of acoustic switches, we present the programmability of the bandgap size and location for the (i) Miura-ori strip in Fig. 7b and c, respectively, and for the (ii) eggbox strip in Fig. 7e and f, respectively. It is clear that both Miura-ori and eggbox strips can be employed as acoustic switches that are highly programmable and tunable.

4.2. Miura-ori and eggbox sheets

Next, we consider the design of Miura-ori and eggbox sheets shown in Fig. 1. The projected nodal unit cell representations along with the associated lumped masses for the Miura-ori and eggbox sheets are shown in Fig. 8a and b, respectively. For both structures, the unit cell contains $M = 4$ nodes and therefore 12 degrees of freedom (DOFs). Every node in Miura-ori is connected to 6 bars, whereas in eggbox one set of nodes is connected to 8 bars each and the other set is connected to 4 bars. The IBZ consists for the rectangle $\{O, P, Q, R\}$ shown in Fig. 5c, obtained after applying time-reversal and vertical inversion symmetries on the BZ (rectangle $\{Q'', Q', Q, R'\}$). On performing a preliminary Bloch wave analysis, we have found that the number and size of bandgaps in Miura-ori and eggbox sheets is rather limited compared to their strip counterparts.

[9] We developed a tailored MATLAB (MATLAB, 1998) computer code for Bloch wave analysis based on the bar-and-hinge model.

[10] For the range of reconfigurability (i.e., varying θ) considered in this work, we have observed that on applying appropriate deformations, the bandgaps in the lower part of the spectrum for the Miura-ori and eggbox structures can be closed (i.e., zero bandgap).

[11] Indeed, depending on the application of interest, different thresholding functions can be employed.

[12] The first 4 bands involve the zero energy rigid body modes at long wavelength limits, i.e., $k \to 0$

[13] We define the location of the bandgap to be the normalized frequency corresponding to the middle of the bandgap. For example, the mean normalized frequency for the bandgap between fourth and fifth bands would be $(\hat{\omega}_4^{max} + \hat{\omega}_5^{min})/2$, where $\hat{\omega}_4^{max}$ and $\hat{\omega}_5^{min}$ correspond to the maximum and minimum of bands 4 and 5, respectively.

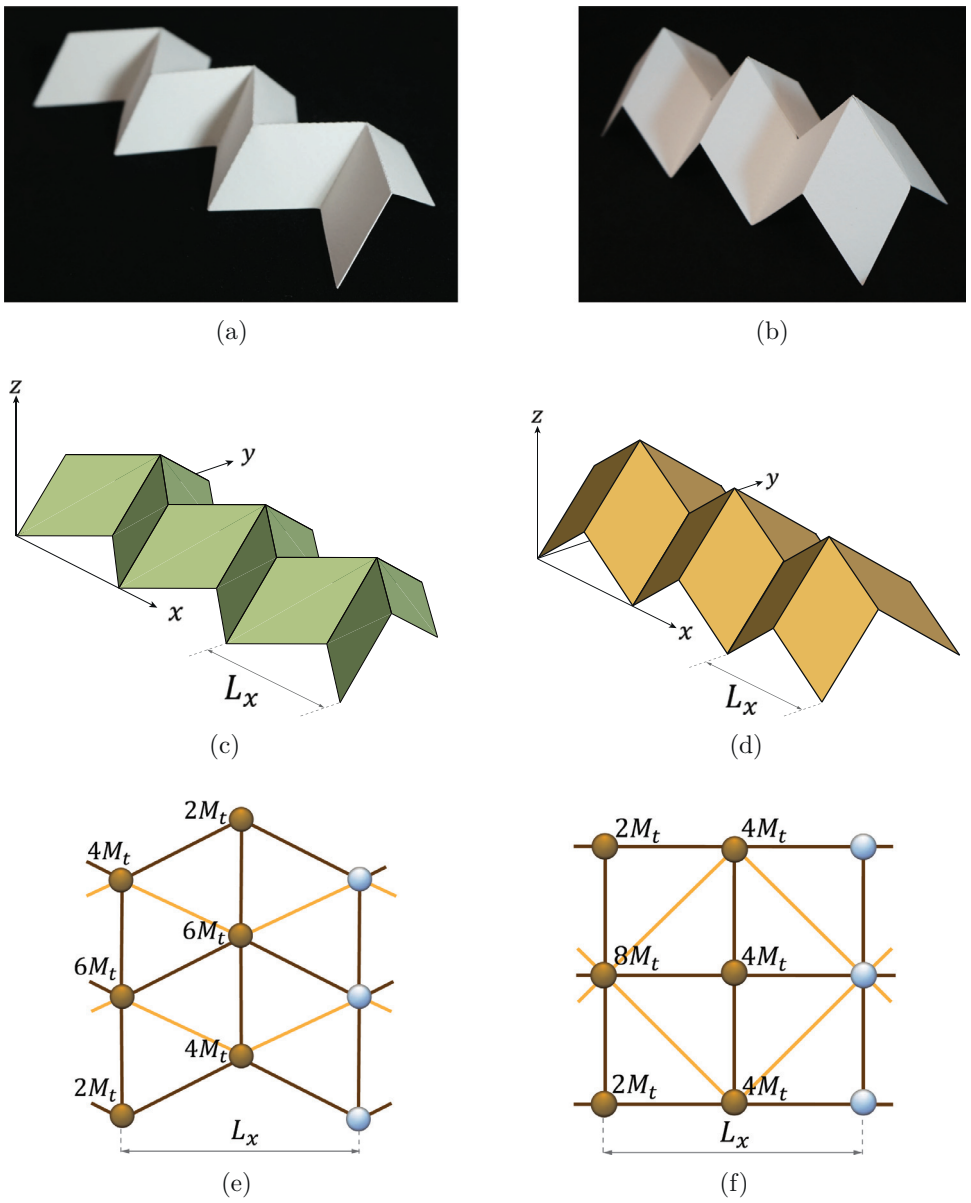

Fig. 6. One-dimensional origami strips. (a), (c), and (e) Paper model, corresponding schematic of a 1×3 Miura-ori origami pattern, and projected lumped mass representation of its unit cell, respectively. (b), (d), and (f) Paper model, corresponding schematic of a 1×3 eggbox origami pattern, and projected lumped mass representation of its unit cell, respectively. (e) and (f) Note that $M_t = M_p/6$, where M_t denotes a third of the triangle mass and M_p is the panel mass. Nodes in darker color belong to the actual unit cell and those in lighter color belong to the neighboring unit cell. (For interpretation of the references to color in this figure legend, the reader is referred to the web version of this article.)

In addition, the bandgaps are located at higher frequencies. A possible explanation for these observations is that the periodicity in both directions endows the sheets with more homogeneity compared to their strip counterparts, which makes them less susceptible to significant bandgaps (Appendix B).

After utilizing the design procedure described previously, we obtain optimized structures with the following parameters: (i) $\alpha = 59.35^\circ$, $b = 4.96$, and $\theta = 57.93^\circ$ for Miura-ori, and (ii) $\alpha = 58.67^\circ$, $b = 5$, and $\theta = 46.67^\circ$ for the eggbox sheets, with bandgaps of 0.51 and 0.59 occurring between the eighth and ninth bands,[14] respectively. The band structure diagrams for these structures are presented in Fig. 9. We find that mode 8 is dominated by axial deformations from bars with length $b = 5$ whereas mode 9 is dominated by axial deformations from bars with length $a = 1$. Since shorter length leads to higher axial stiffness, a bandgap results between modes 8 and 9. For the optimized Miura-ori and eggbox structures, we present

[14] The first 3 bands involve the zero energy rigid body modes at long wavelength limits, i.e., $k \to 0$.

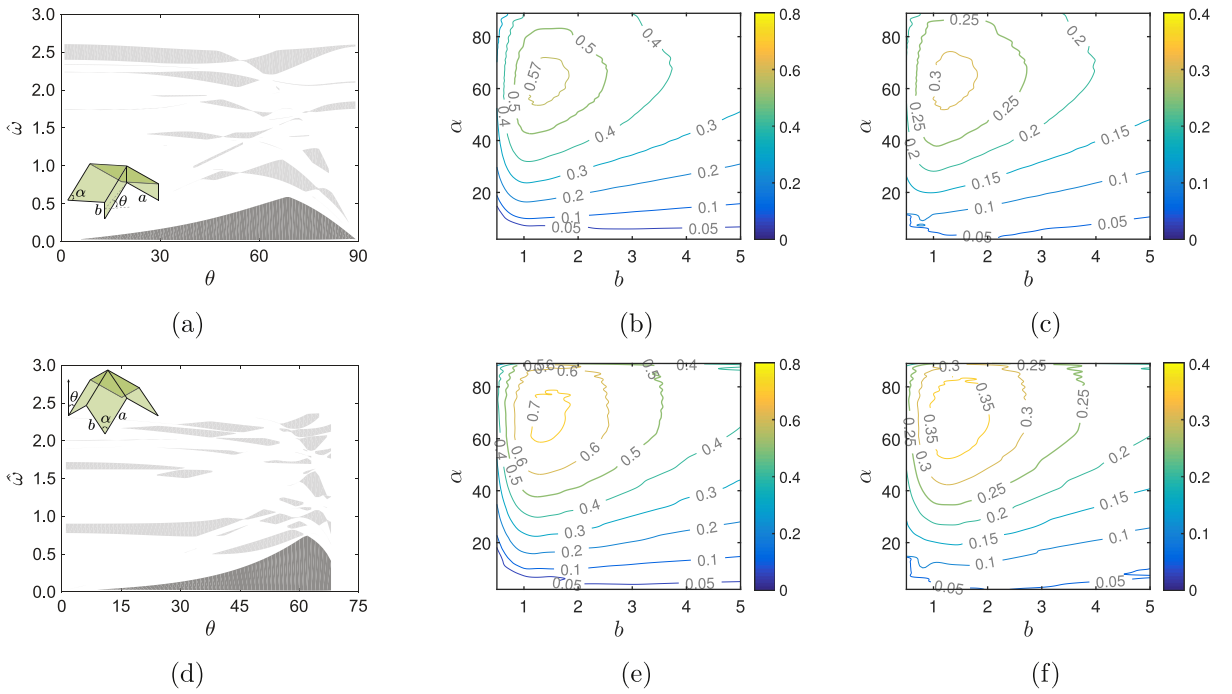

Fig. 7. (a) Tunability of the bandgap size and location for the optimized Miura-ori strip ($\alpha = 64.19^\circ$, $b = 1.09$, and $\theta = 68.64^\circ$). (b) and (c) Programmability of the Miura-ori strip as an acoustic switch in terms of bandgap size and location, respectively. (d) Tunability of the bandgap size and location for the optimized eggbox strip ($\alpha = 69.64^\circ$, $b = 1.4$, and $\theta = 61.87^\circ$). (e) and (f) Programmability of the eggbox strip as an acoustic switch in terms of bandgap size and location, respectively. Note that the darker shade in (a) and (d) is used to highlight the bandgap of interest, for which the programmability is studied in (b), (c) and (e), (f), respectively.

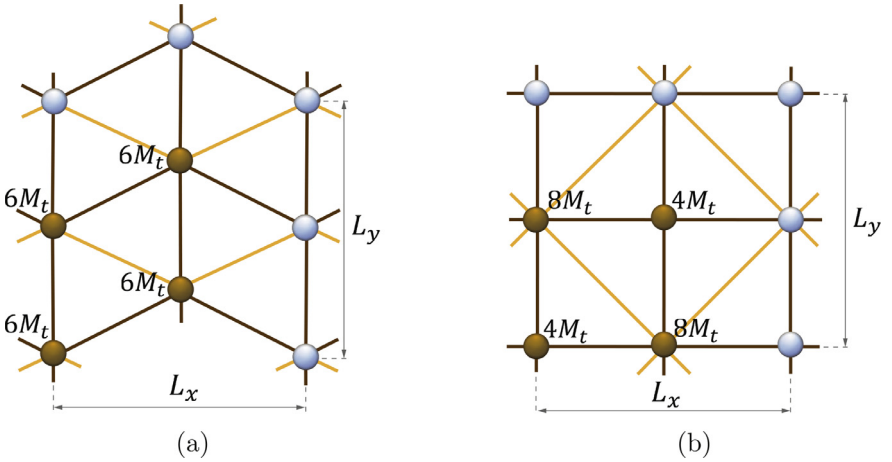

Fig. 8. Projected nodal lumped mass representations for (a) Miura-ori and (b) eggbox planar unit cells. Notice that $M_t = M_p/6$, where M_t denotes a third of the triangle mass and M_p is the panel mass.

the tunability of the bandgap size and location in Fig. 10a and d, respectively (bandgap of interest highlighted using a darker shade). Further, in the context of acoustic switches, we present the programmability of the bandgap size and location for the (i) Miura-ori sheet in Fig. 10b and c, respectively, and for the (ii) eggbox sheet in Fig. 10e and f, respectively. It is clear that both Miura-ori and eggbox sheets can also be employed as acoustic switches that are highly programmable and tunable.

4.3. Composite Miura-ori and eggbox sheets

In the above subsection, we have designed Miura-ori and eggbox sheets that can be utilized as acoustic switches. However, the associated bandgap occurs at higher frequencies relative to the Miura-ori and eggbox strips. To overcome this

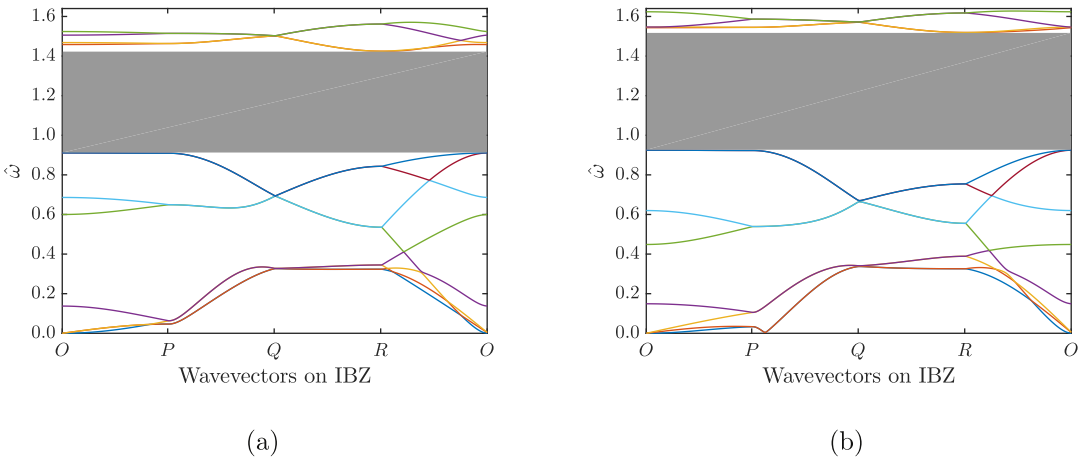

Fig. 9. Band structure diagrams of optimized origami planar configurations: (a) Miura-ori with $\alpha = 59.35^\circ$, $b = 4.96$, and $\theta = 57.93^\circ$. (b) Eggbox with $\alpha = 58.67^\circ$, $b = 5$, and $\theta = 46.67^\circ$. The parameters α, b, and θ are illustrated by Fig. 2. The shaded region illustrates the bandgap.

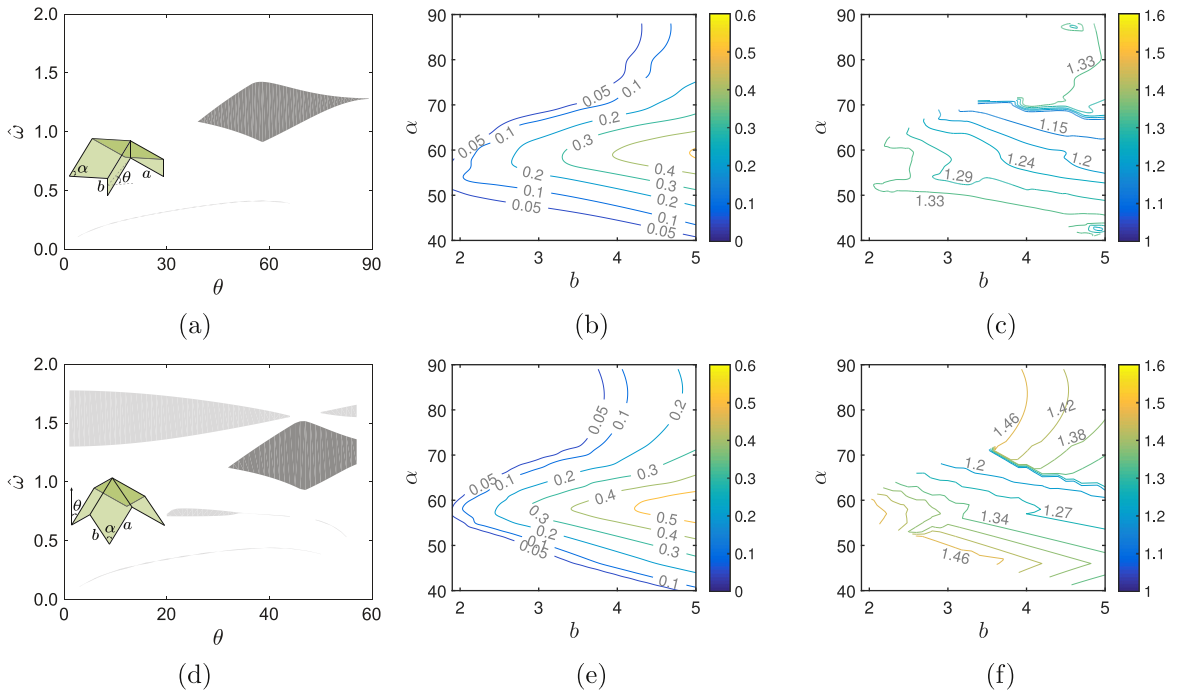

Fig. 10. (a) Tunability of the bandgap size and location for the optimized Miura-ori sheet ($\alpha = 59.35^\circ$, $b = 4.96$, and $\theta = 57.93^\circ$). (b) and (c) Programmability of the Miura-ori sheet as an acoustic switch in terms of bandgap size and location, respectively. (d) Tunability of the bandgap size and location for the optimized eggbox sheet ($\alpha = 58.67^\circ$, $b = 5$, and $\theta = 46.67^\circ$). (e) and (f) Programmability of the eggbox sheet as an acoustic switch in terms of bandgap size and location, respectively. Note that the darker shade in (a) and (d) is used to highlight the bandgap of interest, for which the programmability is studied in (b), (c) and (e), (f), respectively.

limitation, we now enhance the design space by considering *composite* Miura-ori and eggbox sheets,[15] wherein the panels are made up of one of two materials. These materials are denoted by green/red and yellow/red colors in the Miura-ori and eggbox structures, respectively. The mass, axial stiffness and rotational stiffnesses of the green/yellow panels are M_p, K_e, K_b, and K_f, respectively. The corresponding values for the red panels are M_p', K_e', K_b' , and K_f, respectively.[16] For simplicity, we assume that the relative bending stiffness between the red and green/yellow panels is the same as that of their relative axial

[15] Composite origami structures have recently been considered by Boatti et al. (2017) as possible systems with tunable thermal expansion.

[16] In order to retain the foldability of the structure, we assume that the rotational stiffness of the fold lines is uniform throughout the system.

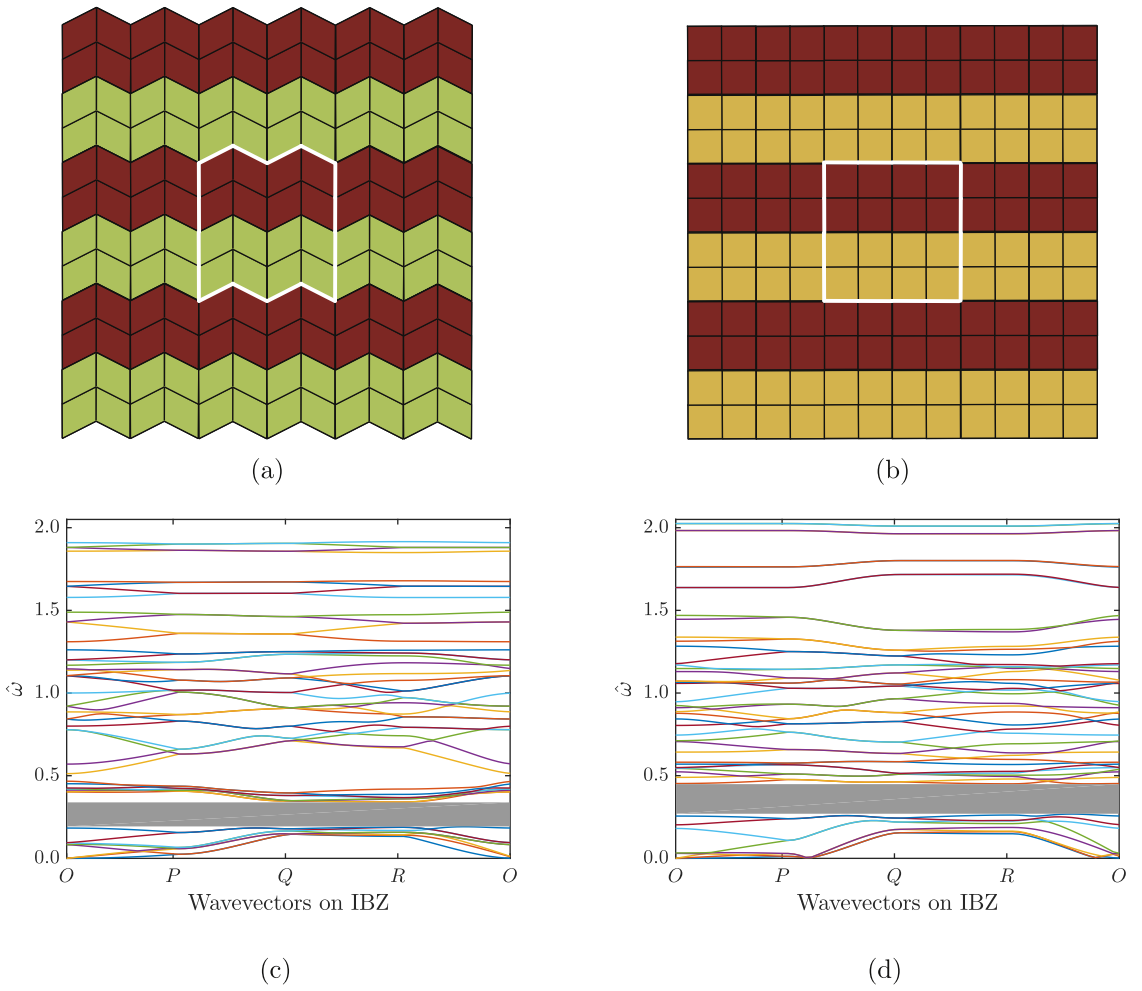

Fig. 11. (a) Projection of the optimized composite Miura-ori sheet with $\alpha = 57.92^\circ$, $b = 3.21$, and $\theta = 51.29^\circ$ – see Fig. 2 for geometric parameters. (b) Projection of the optimized composite eggbox sheet with $\alpha = 74.26^\circ$, $b = 2.92$ and $\theta = 66.47^\circ$ – see Fig. 2 for geometric parameters. (c) Band structure diagram for the optimized composite Miura-ori sheet. (d) Band structure diagram for the optimized composite eggbox sheet.

stiffness, i.e., $K_b'/K_b = K_e'/K_e$. In addition, the axial stiffness of bars along fold lines common to both red and green/yellow panels are assigned the value $(K_e' + K_e)/2$.

In order to be able to study composite origami structures, we generalize the aforementioned design framework by enhancing the design variable space. Specifically, we include the material type of the panels as a binary vector, and thereafter utilize the mixed integer optimization feature of the genetic algorithms. The number of unit cells in the simulation domain is fixed to be four,[17] and the material contrast ratios (M_p'/M_p and K_e'/K_e) are chosen as parameters within the simulation. Since larger K_e'/K_e and smaller M_p'/M_p ratios typically scale the normalized frequencies, while simultaneously increasing the bandgap, we fix the material contrast ratios to be equal (i.e., $M_p'/M_p = K_e'/K_e = 5$.[18])

After using the above described design procedure, we obtain optimized structures with the following parameters: (i) $\alpha = 57.92^\circ$, $b = 3.21$, and $\theta = 51.29^\circ$ for Miura-ori, and (ii) $\alpha = 74.26^\circ$, $b = 2.92$, and $\theta = 66.47^\circ$ for the eggbox sheets, with bandgaps of 0.15 and 0.18 occurring between the eighth and ninth bands respectively. The optimized designs and the corresponding band structure diagrams are shown in Fig. 11. Notably, the location of the bandgaps in the composites occur at much lower part of the spectrum compared to their homogeneous counterparts. For these optimized composite structures, we present the tunability of the bandgap size and location in Fig. 12a and d, respectively (bandgap of interest highlighted using a darker shade). Further, in the context of acoustic switches, we present the programmability of the bandgap size and location for the (i) composite Miura-ori sheet in Fig. 12b and c, respectively, and for the (ii) composite eggbox sheet

[17] We have found that increasing the number of unit cells does not make any significant difference in the results.

[18] This can be varied based on the application of interest. Extremely high contrast ratios are practically feasible by employing lattice based cellular solid materials (Gibson and Ashby, 1999)

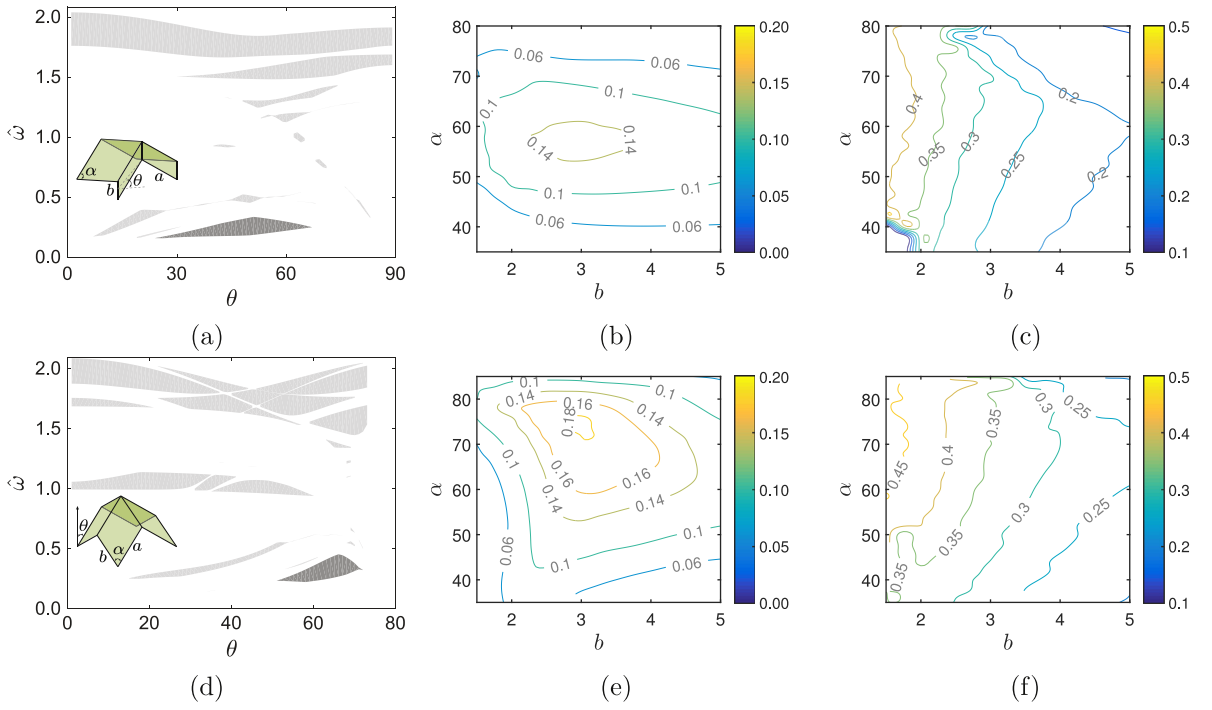

Fig. 12. (a) Tunability of the bandgap size and location for the optimized composite Miura-ori sheet ($\alpha = 57.92^\circ$, $b = 3.21$, and $\theta = 51.29^\circ$). (b) and (c) Programmability of the composite Miura-ori sheet as an acoustic switch in terms of bandgap size and location, respectively. (d) Tunability of the bandgap size and location for the optimized composite eggbox sheet ($\alpha = 74.26^\circ$, $b = 2.92$ and $\theta = 66.47^\circ$). (e) and (f) Programmability of the composite eggbox sheet as an acoustic switch in terms of bandgap size and location, respectively. Note that the darker shade in (a) and (d) is used to highlight the bandgap of interest, for which the programmability is studied in (b), (c) and (e), (f), respectively.

in Fig. 12e and f, respectively. It is clear that both composite Miura-ori and eggbox sheets can be employed as acoustic switches that are highly programmable and tunable.

5. Concluding remarks

In this work, we have developed a generalized Bloch wave framework for the dynamic analysis of structures with nonlocal interactions and have applied it to the design of origami acoustic metamaterials. Specifically, we have discretized the origami structures using a structural bar-and-hinge model that minimizes the degrees of freedom for such structures, without significant loss of accuracy. Observing that this discretization results in nonlocal structural interactions—the stiffness matrix has nonzeros between nodes that are not nearest neighbors due to the coupled deformations arising during folding or bending—we have generalized the traditional Bloch wave method used in structural analysis to enable the study of such systems. Utilizing this framework, while choosing the geometry of the unit cell and the folded state of the structure as design variables, we have designed tunable and programmable Miura-ori and eggbox *strips, sheets*, and *composites* that are large band, low frequency acoustic switches. In doing so, we have demonstrated that the number of bandgaps in the sheets is significantly smaller than their strip counterparts and occurs at relatively higher frequencies, a limitation overcome by considering composite structures that have individual panels made of different materials. In addition, we have found that all the dispersion bands for homogeneous and composite sheets involve wave propagation modes with significant axial deformations.

In summary, our findings indicate that origami-based patterns can be engineered as acoustic metamaterials that are useful in applications like noise control, vibration isolation, impact absorption, and wave guides. In this work, we have restricted our explorations to Miura-ori and eggbox origami patterns. Due to the characteristic deformations (which are predominantly axial) that are required for wave propagation in these patterns (especially in the case of sheets), the range of frequencies that we can target to create bandgaps is limited. Hence, future research could target the design origami patterns that can achieve bandgaps at any desired range of frequencies. Also, design of origami patterns with other properties (e.g., thermal bandgaps) could enhance the capabilities of origami assemblages as multifunctional materials. The presence of bulk bandgaps in the origami structures opens new avenues to investigate and design patterns with topologically protected modes (Chen et al., 2016; Huber, 2016) which are useful in applications like waveguiding and acoustic cloaking. The aforementioned possibilities can be extended from origami with parallelogram panels (used in this investigation) to origami with polygonal panels.

Acknowledgments

GP and PP acknowledge support from the National Science Foundation (NSF) through grant CMMI 1538830, and from the endowment provided by the Raymond Allen Jones Chair at the Georgia Institute of Technology. We acknowledge useful interactions with Prof. Katia Bertoldi, which helped us in discovering the presence of bandgaps in 2D homogeneous Miura-ori sheets.

Appendix A. Bloch wave analysis of a monoatomic chain with nonlocal interactions

In this appendix, we demonstrate that in order to accurately analyze periodic structural systems with nonlocal interactions, a generalization of the commonly adopted Bloch wave analysis is required, akin to the one presented in Section 3. As a representative example, we choose the monoatomic chain shown in Fig. A.13, wherein the interactions are up to second nearest neighbors. We denote the mass by M_1, the stiffnesses of the springs between the first and second nearest neighbors by K_1 and K_2, respectively, and the length of the unit cell (i.e., distance between the masses) by L_0.

Consider a system comprising of N unit cells of the above described monoatomic chain. The associated stiffness matrix $\mathbf{K} \in \mathbb{R}^{N\times N}$ is of the form

$$\mathbf{K} = \begin{bmatrix} (2K_1+2K_2) & -K_1 & -K_2 & 0 & \dots & \dots & 0 & -K_2 & -K_1 \\ -K_1 & (2K_1+2K_2) & -K_1 & -K_2 & 0 & \dots & \dots & 0 & -K_2 \\ -K_2 & -K_1 & (2K_1+2K_2) & -K_1 & -K_2 & 0 & \dots & \dots & 0 \\ \dots & \dots & \dots & \dots & \dots & \dots & \dots & \dots & \dots \\ \dots & \dots & \dots & \dots & \dots & \dots & \dots & \dots & \dots \\ \dots & \dots & \dots & \dots & \dots & \dots & \dots & \dots & \dots \\ \dots & \dots & \dots & \dots & \dots & \dots & \dots & \dots & \dots \\ \dots & \dots & \dots & \dots & \dots & \dots & \dots & \dots & \dots \\ -K_1 & -K_2 & 0 & \dots & \dots & 0 & -K_2 & -K_1 & (2K_1+2K_2) \end{bmatrix}, \tag{A.1}$$

and the mass matrix $\mathbf{M} \in \mathbb{R}^{N\times N}$ is of the form

$$\mathbf{M} = \begin{bmatrix} M_1 & 0 & 0 & \dots & \dots & \dots & 0 & 0 \\ 0 & M_1 & 0 & 0 & \dots & \dots & \dots & 0 \\ 0 & 0 & M_1 & 0 & 0 & \dots & \dots & \dots \\ \dots & 0 & 0 & M_1 & 0 & 0 & \dots & \dots \\ \dots & \dots & \dots & \dots & \dots & \dots & \dots & \dots \\ \dots & \dots & \dots & \dots & \dots & \dots & \dots & \dots \\ \dots & \dots & \dots & \dots & 0 & 0 & M_1 & 0 \\ 0 & 0 & \dots & \dots & \dots & 0 & 0 & M_1 \end{bmatrix}. \tag{A.2}$$

It follows from Eq. (15) that

$$\begin{aligned} \tilde{K}_{mm} &= K_{00} + e^{-\mathrm{i}k_m L_0} K_{01} + e^{-\mathrm{i}2k_m L_0} K_{02} + e^{\mathrm{i}k_m L_0} K_{0(-1)} + e^{\mathrm{i}2k_m L_0} K_{0(-2)} \\ &= (2K_1+2K_2) - e^{-\mathrm{i}k_m L_0} K_1 - e^{-\mathrm{i}2k_m L_0} K_2 - e^{\mathrm{i}k_m L_0} K_1 - e^{\mathrm{i}2k_m L_0} K_2, \end{aligned} \tag{A.3}$$

$$\tilde{M}_{mm} = M_1, \tag{A.4}$$

from which we arrive at the following dispersion relation (Eq. (14)):

$$\omega_m^2 = ((2K_1+2K_2) - e^{-\mathrm{i}k_m L_0} K_1 - e^{-\mathrm{i}2k_m L_0} K_2 - e^{\mathrm{i}k_m L_0} K_1 - e^{\mathrm{i}2k_m L_0} K_2)/M_1. \tag{A.5}$$

For this system, if we had instead utilized the standard Bloch wave analysis that is commonly employed in the structural mechanics literature (e.g., Gonella and Ruzzene, 2008; Mousanezhad et al., 2015; Phani et al., 2006; Ruzzene et al., 2003),

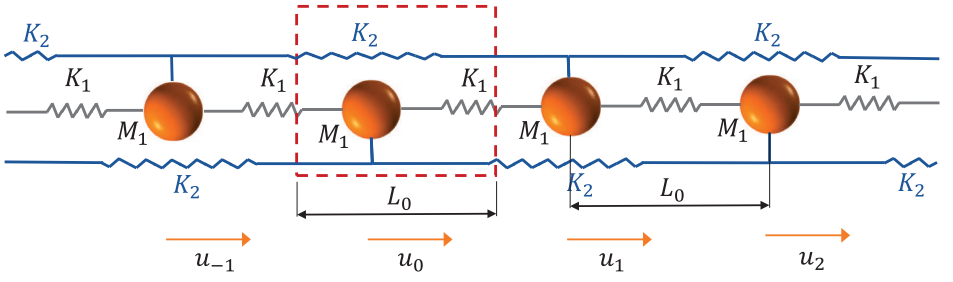

Fig. A.13. Monoatomic chain with nonlocal interactions.

we would have arrived at the following incorrect result:

$$\omega_m^2 = ((2K_1 + 2K_2) - e^{-\mathrm{i}k_m L_0}K_1 - e^{\mathrm{i}k_m L_0}K_1)/M_1. \tag{A.6}$$

This example highlights the need for the generalized Bloch wave analysis developed in Section 3 while analyzing structures possessing nonlocal interactions.

Appendix B. Effect of inhomogeneity on the diatomic chain's bandgap

In this appendix, we study the effect of inhomogeneity on the bandgap of the diatomic chain shown in Fig. B.14. We denote the alternating masses by M_1 and M_2, the stiffnesses of the alternating springs by K_1 and K_2, and the length of the unit cell by L_0. Proceeding as in Section 3, consider a system comprising of N unit cells of the diatomic chain. The associated stiffness matrix $\mathbf{K} \in \mathbb{R}^{N\times N}$ is of the form

$$\mathbf{K} = \begin{bmatrix} (K_1+K_2) & -K_1 & 0 & \dots & \dots & \dots & 0 & -K_2 \\ -K_1 & (K_1+K_2) & -K_2 & 0 & \dots & \dots & \dots & 0 \\ 0 & -K_2 & (K_1+K_2) & -K_1 & 0 & \dots & \dots & \dots \\ \dots & 0 & -K_1 & (K_1+K_2) & -K_2 & 0 & \dots & \dots \\ \dots & \dots & \dots & \dots & \dots & \dots & \dots & \dots \\ \dots & \dots & \dots & \dots & \dots & \dots & \dots & \dots \\ \dots & \dots & \dots & \dots & 0 & -K_2 & (K_1+K_2) & -K_1 \\ -K_2 & 0 & \dots & \dots & \dots & 0 & -K_1 & (K_1+K_2) \end{bmatrix}, \tag{B.1}$$

and the mass matrix $\mathbf{M} \in \mathbb{R}^{N\times N}$ is of the form

$$\mathbf{M} = \begin{bmatrix} M_1 & 0 & 0 & \dots & \dots & \dots & 0 & 0 \\ 0 & M_2 & 0 & 0 & \dots & \dots & \dots & 0 \\ 0 & 0 & M_1 & 0 & 0 & \dots & \dots & \dots \\ \dots & 0 & 0 & M_2 & 0 & 0 & \dots & \dots \\ \dots & \dots & \dots & \dots & \dots & \dots & \dots & \dots \\ \dots & \dots & \dots & \dots & \dots & \dots & \dots & \dots \\ \dots & \dots & \dots & \dots & 0 & 0 & M_1 & 0 \\ 0 & 0 & \dots & \dots & \dots & 0 & 0 & M_2 \end{bmatrix}. \tag{B.2}$$

It follows from Eq. (15) that

$$\tilde{\mathbf{K}}_{\mathbf{mm}} = \begin{bmatrix} K_1+K_2 & -K_1 - K_2 e^{\mathrm{i}k_{\mathbf{m}}L_0} \\ -K_1 - K_2 e^{-\mathrm{i}k_{\mathbf{m}}L_0} & K_1+K_2 \end{bmatrix}, \qquad \tilde{\mathbf{M}}_{\mathbf{mm}} = \begin{bmatrix} M_1 & 0 \\ 0 & M_2 \end{bmatrix}, \tag{B.3}$$

from which we arrive at the following dispersion relation (Eq. (14)):

$$\omega_m^2 - \omega_m \frac{(K_1+K_2)(M_1+M_2)}{M_1 M_2} + 4\frac{K_1 K_2}{M_1 M_2}\sin^2(k_{\mathbf{m}}L_0/2) = 0. \tag{B.4}$$

Thereafter, the normalized bandgap for this system can be written as

$$\hat{\delta} = \sqrt{(1+\kappa)(1+\gamma) + \sqrt{(1+\kappa)^2(1+\gamma)^2 - 16(\gamma\kappa)}} - \sqrt{(1+\kappa)(1+\gamma) - \sqrt{(1+\kappa)^2(1+\gamma)^2 - 16(\gamma\kappa)}}, \tag{B.5}$$

where $\hat{\delta} = \delta/\sqrt{K_1/M_1}$ with δ being the bandgap, $\kappa = K_2/K_1$ is the stiffness ratio, and $\gamma = M_1/M_2$ is the mass ratio. We plot the resulting contours of $\hat{\delta}$ in Fig. B.15, from which it is clear that the bandgaps become larger as the stiffness and mass ratios become larger. Indeed, when the system is homogeneous (i.e., $\kappa = \gamma = 1$), there is no bandgap. This example suggests that bandgaps are likely to be larger in systems that are more inhomogeneous.

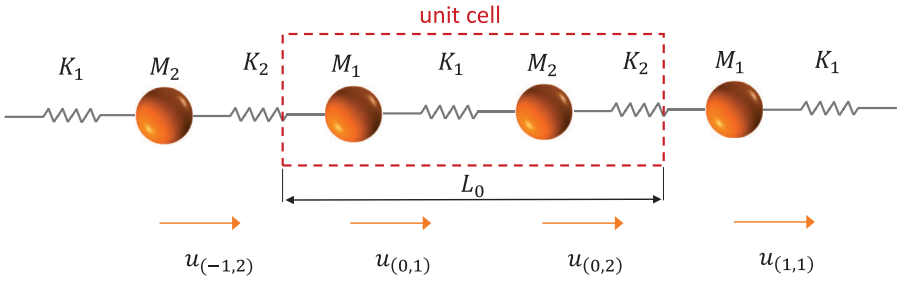

Fig. B.14. Diatomic chain.

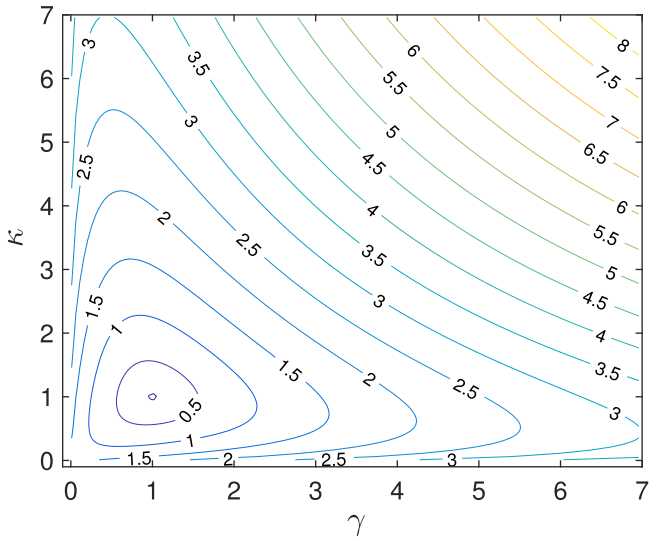

Fig. B.15. Contours of bandgap in a diatomic chain as a function of the stiffness ratio κ and mass ratio γ.

References

Aghaei, A., Dayal, K., Elliott, R.S., 2013. Symmetry-adapted phonon analysis of nanotubes. J. Mech. Phys. Solids 61 (2), 557–578.
Baravelli, E., Ruzzene, M., 2013. Internally resonating lattices for bandgap generation and low-frequency vibration control. J. Sound Vib. 332 (25), 6562–6579.
Bertoldi, K., Boyce, M., 2008. Mechanically triggered transformations of phononic band gaps in periodic elastomeric structures. Phys. Rev. B 77 (5), 052105.
Boatti, E., Vasios, N., Bertoldi, K., 2017. Origami metamaterials for tunable thermal expansion. Adv. Mater. 29 (26), 1700360.
Brillouin, L., 1953. Wave Propagation in Periodic Structures: Electric Filters and Crystal Lattices. Dover Publications.
Chen, B.G.-g., Liu, B., Evans, A.A., Paulose, J., Cohen, I., Vitelli, V., Santangelo, C., 2016. Topological mechanics of origami and kirigami. Phys. Rev. Lett. 116 (13), 135501.
Christensen, J., Kadic, M., Kraft, O., Wegener, M., 2015. Vibrant times for mechanical metamaterials. MRS Commun. 5 (03), 453–462.
Cummer, S.A., Christensen, J., Alù, A., 2016. Controlling sound with acoustic metamaterials. Nat. Rev. Mater. 1 (3), 16001.
Del Grosso, A., Basso, P., 2010. Adaptive building skin structures. Smart Mater. Struct. 19 (12), 124011.
Demaine, E.D., O'Rourke, J., 2007. Geometric Folding Algorithms. Cambridge University Press, Cambridge.
Eidini, M., Paulino, G.H., 2015. Unraveling metamaterial properties in zigzag-base folded sheets. Sci. Adv. 1 (8), e1500224.
Evans, A.A., Silverberg, J.L., Santangelo, C.D., 2015. Lattice mechanics of origami tessellations. Phys. Rev. E 92 (1), 013205.
Felton, S., Tolley, M., Demaine, E., Rus, D., Wood, R., 2014. A method for building self-folding machines. Science 345 (6197), 644–646.
Filipov, E.T., Liu, K., Tachi, T., Schenk, M., Paulino, G.H., 2017. Bar and hinge models for scalable analysis of origami. Int. J. Solids Struct. 124, 26–45.
Filipov, E.T., Tachi, T., Paulino, G.H., 2015a. Origami tubes assembled into stiff, yet reconfigurable structures and metamaterials. Proc. Natl. Acad. Sci. 112 (40), 12321–12326.
Filipov, E.T., Tachi, T., Paulino, G.H., 2015b. Toward optimization of stiffness and flexibility of rigid, flat-foldable origami structures. In: Origami6: Proceedings of the Sixth International Meeting on Origami Science, Mathematics and Education, pp. 409–419.
Gibson, L.J., Ashby, M.F., 1999. Cellular Solids: Structure and Properties. Cambridge University Press.
Gonella, S., Ruzzene, M., 2008. Analysis of in-plane wave propagation in hexagonal and re-entrant lattices. J. Sound Vib. 312 (1), 125–139.
Gottfried, K., Yan, T.-M., 2013. Quantum Mechanics: Fundamentals. Springer Science & Business Media.
Huber, S.D., 2016. Topological mechanics. Nat. Phys. 12 (7), 621–623.
Hussein, M.I., Leamy, M.J., Ruzzene, M., 2014. Dynamics of phononic materials and structures: historical origins, recent progress, and future outlook. Appl. Mech. Rev. 66 (4), 040802.
Karner, H., Schneid, J., Ueberhuber, C.W., 2003. Spectral decomposition of real circulant matrices. Linear Algebra Appl. 367, 301–311.
Kerszberg, N., Suryanarayana, P., 2015. Ab initio strain engineering of graphene: opening bandgaps up to 1 ev. RSC Adv. 5 (54), 43810–43814.
Kittel, C., 1966. Introduction to Solid State Physics. John Wiley & Sons.
Kuribayashi, K., Tsuchiya, K., You, Z., Tomus, D., Umemoto, M., Ito, T., Sasaki, M., 2006. Self-deployable origami stent grafts as a biomedical application of Ni-rich TiNi shape memory alloy foil. Mater. Sci. Eng. A 419 (1), 131–137.
Lang, R.J., 2011. Origami Design Secrets: Mathematical Methods for an Ancient Art. AK Peters, Natick, MA.
Liu, Z., Zhang, X., Mao, Y., Zhu, Y., Yang, Z., Chan, C., Sheng, P., 2000. Locally resonant sonic materials. Science 289 (5485), 1734–1736.
Maldovan, M., 2013. Sound and heat revolutions in phononics. Nature 503 (7475), 209–217.
MATLAB, 1998. MATLAB Users Guide. The MathWorks Inc., Natick, MA.
Miura, K., 1985. Method of packaging and deployment of large membranes in space. Inst. Space Astronaut. Sci. Rep. 618, 1.
Mousanezhad, D., Babaee, S., Ghosh, R., Mahdi, E., Bertoldi, K., Vaziri, A., 2015. Honeycomb phononic crystals with self-similar hierarchy. Phys. Rev. B 92 (10), 104304.
Mu, J., Hou, C., Wang, H., Li, Y., Zhang, Q., Zhu, M., 2015. Origami-inspired active graphene-based paper for programmable instant self-folding walking devices. Sci. Adv. 1 (10), e1500533.
Nash, L.M., Kleckner, D., Read, A., Vitelli, V., Turner, A.M., Irvine, W.T., 2015. Topological mechanics of gyroscopic metamaterials. Proc. Natil. Acad. Sci. 112 (47), 14495–14500.
Olson, B.J., Shaw, S.W., Shi, C., Pierre, C., Parker, R.G., 2014. Circulant matrices and their application to vibration analysis. Appl. Mech. Rev. 66 (4), 040803.
ORourke, J., 2011. How to Fold it: The Mathematics of Linkages, Origami, and Polyhedra. Cambridge University Press.
Ota, N., Wilson, L., Neto, A.G., Pellegrino, S., Pimenta, P., 2016. Nonlinear dynamic analysis of creased shells. Finite Elem. Anal. Des. 121, 64–74.
Pal, R.K., Ruzzene, M., 2017. Edge waves in plates with resonators: an elastic analogue of the quantum valley Hall effect. New J. Phys. 19 (2), 025001.
Peraza-Hernandez, E.A., Hartl, D.J., Malak Jr, R.J., Lagoudas, D.C., 2014. Origami-inspired active structures: a synthesis and review. Smart Mater. Struct. 23 (9), 094001.
Phani, A.S., Woodhouse, J., Fleck, N., 2006. Wave propagation in two-dimensional periodic lattices. J. Acoust. Soc. Am. 119 (4), 1995–2005.

Pratapa, P.P., Suryanarayana, P., 2016. On numerically predicting the onset and mode of instability in atomistic systems. Mech. Res. Commun. 78, 27–33. Recent Advances in Multiscale, Multifunctional and Functionally Graded Materials.
Pratapa, P.P., Suryanarayana, P., Paulino, G.H., 2017. Design of Miura-ori patterns with acoustic bandgaps. In: ASME 2017 International Design Engineering Technical Conferences and Computers and Information in Engineering Conference. American Society of Mechanical Engineers. V05BT07A012–V05BT07A012.
Rjasanow, S., 1994. Effective algorithms with circulant-block matrices. Linear Algebra Appl. 202, 55–69.
Ruzzene, M., Scarpa, F., Soranna, F., 2003. Wave beaming effects in two-dimensional cellular structures. Smart Mater. Struct. 12 (3), 363.
Ryu, J., DAmato, M., Cui, X., Long, K.N., Qi, H.J., Dunn, M.L., 2012. Photo-origami–Bending and folding polymers with light. Appl. Phys. Lett. 100 (16), 161908.
Schenk, M., 2011. Folded Shell Structures. University of Cambridge. Ph.D. thesis.
Schenk, M., Guest, S.D., 2011. Origami folding: A structural engineering approach. In: Origami5: Proceedings of the Fifth International Meeting on Origami Science, Mathematics, and Education. CRC Press, Boca Raton, FL, pp. 291–304.
Schenk, M., Guest, S.D., 2013. Geometry of Miura-folded metamaterials. Proc. Natl. Acad. Sci. 110 (9), 3276–3281.
Silverberg, J.L., Evans, A.A., McLeod, L., Hayward, R.C., Hull, T., Santangelo, C.D., Cohen, I., 2014. Using origami design principles to fold reprogrammable mechanical metamaterials. Science 345 (6197), 647–650.
Song, Z., Ma, T., Tang, R., Cheng, Q., Wang, X., Krishnaraju, D., Panat, R., Chan, C.K., Yu, H., Jiang, H., 2014. Origami lithium-ion batteries. Nat. Commun. 5.
Suryanarayana, P., 2013. Optimized purification for density matrix calculation. Chem. Phys. Lett. 555, 291–295.
Suryanarayana, P., Pratapa, P.P., Sharma, A., Pask, J.E., 2017. SQDFT: Spectral Quadrature method for large-scale parallel O (N) Kohn–Sham calculations at high temperature. Comput. Phys. Commun..
Süsstrunk, R., Huber, S.D., 2016. Classification of topological phonons in linear mechanical metamaterials. Proc. Natl. Acad. Sci. 113 (33), E4767–E4775.
Tang, R., Huang, H., Tu, H., Liang, H., Liang, M., Song, Z., Xu, Y., Jiang, H., Yu, H., 2014. Origami-enabled deformable silicon solar cells. Appl. Phys. Lett. 104 (8), 083501.
Waitukaitis, S., van Hecke, M., 2016. Origami building blocks: generic and special four-vertices. Phys. Rev. E 93 (2), 023003.
Wang, P., Lu, L., Bertoldi, K., 2015. Topological phononic crystals with one-way elastic edge waves. Phys. Rev. Lett. 115 (10), 104302.
Wei, Z.Y., Guo, Z.V., Dudte, L., Liang, H.Y., Mahadevan, L., 2013. Geometric mechanics of periodic pleated origami. Phys. Rev. Lett. 110 (21), 215501.
Yasuda, H., Lee, M., Yang, J., 2016. Tunable wave dynamics in origami-based mechanical metamaterials. In: ASME 2016 International Design Engineering Technical Conferences and Computers and Information in Engineering Conference. American Society of Mechanical Engineers. V05BT07A012–V05BT07A012.